Cell

PspA adopts an ESCRT-III-like fold and remodels bacterial membranes

Graphical abstract

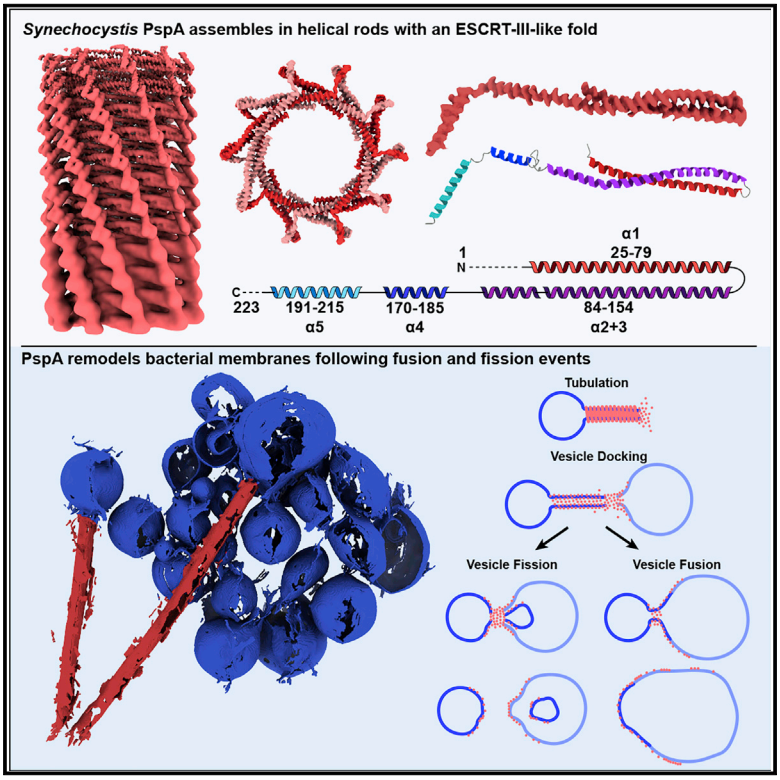

Highlights

- Cryo-EM structure of assembled helical PspA rods
- PspA adopts a canonical ESCRT-III fold
- PspA rods can enclose lipids generating positive membrane curvature
- PspA remodels bacterial membranes following fusion and fission events

Authors

Benedikt Junglas, Stefan T. Huber, Thomas Heidler, ..., Nadja Hellmann, Dirk Schneider, Carsten Sachse

Correspondence

dirk.schneider@uni-mainz.de (D.S.), c.sachse@fz-juelich.de (C.S.)

In brief

Structural and functional characterization of PspA reveals an unkown ESCRT-III family member capable of mediating membrane fission and fusion processes.

Junglas et al., 2021, Cell *184*, 3674–3688
July 8, 2021
https://doi.org/10.1016/j.cell.2021.05.042

CellPress

CellPress

Cell

Article

PspA adopts an ESCRT-III-like fold and remodels bacterial membranes

Benedikt Junglas,[1,2,4] Stefan T. Huber,[3] Thomas Heidler,[1,2] Lukas Schlösser,[4] Daniel Mann,[1,2] Raoul Hennig,[4] Mairi Clarke,[3] Nadja Hellmann,[4] Dirk Schneider,[4,5,*] and Carsten Sachse[1,2,6,7,*]

[1]Ernst-Ruska Centre for Microscopy and Spectroscopy with Electrons, ER-C-3/Structural Biology, Forschungszentrum Jülich, 52425 Jülich, Germany

[2]JuStruct: Jülich Center for Structural Biology, Forschungszentrum Jülich, 52425 Jülich, Germany

[3]European Molecular Biology Laboratory (EMBL), Structural and Computational Biology Unit, Meyerhofstraße 1, 69117 Heidelberg, Germany

[4]Department of Chemistry, Biochemistry, Johannes Gutenberg University Mainz, 55128 Mainz, Germany

[5]Institute of Molecular Physiology, Johannes Gutenberg University Mainz, 55128 Mainz, Germany

[6]Department of Biology, Heinrich Heine University, Universitätsstr. 1, 40225 Düsseldorf, Germany

[7]Lead contact

*Correspondence: dirk.schneider@uni-mainz.de (D.S.), c.sachse@fz-juelich.de (C.S.)

https://doi.org/10.1016/j.cell.2021.05.042

SUMMARY

PspA is the main effector of the phage shock protein (Psp) system and preserves the bacterial inner membrane integrity and function. Here, we present the 3.6 Å resolution cryoelectron microscopy (cryo-EM) structure of PspA assembled in helical rods. PspA monomers adopt a canonical ESCRT-III fold in an extended open conformation. PspA rods are capable of enclosing lipids and generating positive membrane curvature. Using cryo-EM, we visualized how PspA remodels membrane vesicles into μm-sized structures and how it mediates the formation of internalized vesicular structures. Hotspots of these activities are zones derived from PspA assemblies, serving as lipid transfer platforms and linking previously separated lipid structures. These membrane fusion and fission activities are in line with the described functional properties of bacterial PspA/IM30/LiaH proteins. Our structural and functional analyses reveal that bacterial PspA belongs to the evolutionary ancestry of ESCRT-III proteins involved in membrane remodeling.

INTRODUCTION

Membrane remodeling and re-shaping is crucial for cell viability in all domains of life. In order to maintain the integrity of internal membranes under conditions such as heat stress, osmotic stress, organic solvents, or phage infections, many bacteria activate the phage shock protein (Psp) system (Brissette et al., 1990; Kobayashi et al., 1998; Weiner et al., 1991). The currently best studied *E. coli* Psp-system consists of seven genes: the *pspABCDE* operon, the regulation factor *pspF*, and the effector *pspG* (Brissette et al., 1991; Elderkin et al., 2002; Lloyd et al., 2004). The Psp response is triggered during dissipation of the proton motive force and secretin mislocation (Darwin, 2005; Engl et al., 2011; Joly et al., 2010), which both indicate defects in the structure and integrity of the bacterial cytoplasmic membrane. PspA is the key effector of the Psp system, and in *E. coli*, it interacts with the cytoplasmic membrane sensor proteins PspB and PspC (Darwin, 2005; Joly et al., 2010). Free PspA can bind peripherally to bacterial inner membranes by interacting with negatively charged membrane lipids (Jovanovic et al., 2014) and thereby counteracts membrane stress (Joly et al., 2010; Manganelli and Gennaro, 2017). This way, membrane-bound PspA can, for instance, block proton leakage of isolated damaged membranes (Kobayashi et al., 2007). In support, members of the PspA family are thought to tether and seal stress-induced membrane lesions, presumably by triggering lipid bilayer fusion (Siebenaller et al., 2020). Indeed, a membrane fusion activity has been reported previously for the PspA homolog IM30 (inner membrane-associated protein of 30 kDa, alternatively known as Vipp1) of the cyanobacterium *Synechocystis* sp. PCC 6803 (Hennig et al., 2015). More recently, a membrane protecting protein carpet mechanism has been proposed for IM30 (Junglas et al., 2020).

Although the Psp response system appears to be conserved in Gram-negative bacteria, Psp homologs have also been identified in cyanobacteria, archaea as well as in chloroplasts (Manganelli and Gennaro, 2017). Yet, solely homologs of PspA appear to be strictly conserved and thus critical for membrane protection and remodeling (Manganelli and Gennaro, 2017). The homologous proteins PspA, IM30/Vipp1 (chloroplasts and cyanobacteria), and LiaH (*Firmicutes*, *Bacillus*, and *Listeria*) are part of a bacterial membrane remodeling family that shares many structural and functional features for maintaining membrane integrity (Thurotte et al., 2017; Vothknecht et al., 2012). PspA/LiaH/IM30 proteins form large ring and rod-like homo-oligomeric structures (>1 MDa) and share predicted secondary structures and

conserved sequence motifs (Bultema et al., 2010; Fuhrmann et al., 2009; Hankamer et al., 2004; Male et al., 2014; Saur et al., 2017; Theis et al., 2019, 2020; Thurotte et al., 2017; Vothknecht et al., 2012; Wolf et al., 2010). The fragment structure of an extended α-helical hairpin formed by the 2nd and 3rd *Eco*PspA helices was resolved by X-ray crystallography (Osadnik et al., 2015), yet, the full-length PspA structure is still unknown.

Although most membrane-remodeling proteins such as epsin, dynamin, or BAR domain-containing proteins were first identified in eukaryotes (Ford et al., 2002; Frost et al., 2009; Praefcke and McMahon, 2004), membrane remodeling is a common process in all three domains of life. For instance, endosomal sorting complexes required for transport (ESCRT) were originally characterized in eukaryotic membrane trafficking events of multivesicular body biogenesis (Katzmann et al., 2001), viral budding (Garrus et al., 2001), and cytokinesis (Carlton and Martin-Serrano, 2007) with the common topology of moving membrane away from the cytosol. More recently, they have been shown to be involved in a series of diverse membrane remodeling processes in eukaryotic cells, which include nuclear envelope sealing (Vietri et al., 2015), plasma membrane repair, lysosomal protein degradation (Zhu et al., 2017), and closure of autophagosomes (Takahashi et al., 2018; Zhen et al., 2020). Despite this functional diversity, the responsible core proteins belong to a single conserved group of ESCRT-III proteins. ESCRT-III proteins comprise approximately 220 amino acids and share seven predicted α helices (helices α0–α6). Structural analyses of truncated CHMP3 revealed a compact structure made of a four-helix bundle comprising a long α-helical hairpin motif (Muziol et al., 2006). More recently, polymers assembled from full-length ESCRT-III were elucidated at near-atomic resolution using cryoelectron microscopy (cryo-EM): human IST1 and CHMP1B form a hetero-polymer with a compact and extended conformation forming a tubular assembly (McCullough et al., 2015), whereas yeast Vps24 assembles in a double-stranded filament composed of domain-swapped dimers in the extended conformation (Huber et al., 2020). The structures of IST1/CHMP1B tubes confirmed the presence of a lipid bilayer in the lumen of the assemblies (Nguyen et al., 2020). Thus, IST1/CHMP1B is capable of constricting vesicles and inducing positive membrane curvature suitable for opposite ESCRT topology membrane processes. It has been shown that mixing of different ESCRT proteins in a particular order is required to assemble hetero-polymeric complexes that drive membrane remodeling *in vitro* (Huber et al., 2020; Pfitzner et al., 2020). Downstream of the ESCRT-III activity is the AAA-ATPase Vps4 that promotes assembly and disassembly of ESCRT-III complexes and thereby contributes to membrane remodeling (Caillat et al., 2019).

Despite the known critical roles of ESCRT-III proteins in the Archaea and Eukarya kingdom, members of a conserved bacterial ESCRT family have not yet been identified by sequence analysis, structural comparison, or by functional characterization. In the current study, we determined the 3.6 Å resolution cryo-EM structure of PspA assembled in helical tubes. The built atomic model reveals that PspA adopts a canonical ESCRT-III fold making up the wall of the tubular assemblies. When PspA is reconstituted with small lipid vesicles, it induces vesicle growth and formation of internalized membrane structures, indicating membrane fusion as well as fission activities. The cryo-EM structure combined with biochemical lipid remodeling experiments show that bacterial PspA is a bona fide member of an evolutionary conserved ESCRT-III family.

RESULTS

PspA rods are tubular assemblies with helical symmetry

In order to structurally investigate the membrane-protective mechanism of PspA, we overexpressed PspA of the cyanobacterium *Synechocystis* sp. PCC 6803. Expression of a fluorescent *Synechocystis* PspA variant in a Δ*pspA E. coli* strain resulted in the formation of multiple, large PspA assemblies *in vivo*, which were preferably localized at the cell poles (Figure S1A), supporting previous observations of large inner membrane-associated PspA oligomers (Engl et al., 2009; Jovanovic et al., 2014; Yamaguchi et al., 2013). Subsequently, we visualized purified PspA using cryo-EM. The acquired micrographs show elongated rod assemblies with around 20 nm width and varying lengths of up to several hundreds of nanometers (Figure 1A). Closer analysis of the 2D class average from a homogeneous subset (Figures S1B and S1C) revealed a basic Christmas-tree pattern with a longitudinal repeat every 30 Å indicative of a repeating pitch typical for helical assemblies (Figure 1B). The corresponding power spectrum showed a layer line pattern diffracting to approximately 7 Å resolution and revealed the helical organization with a helical rise and rotation of 2.9 Å and 35.3° per subunit (Figures 1C and S1D). Using a total of 139,300 asymmetric units, we then determined the cryo-EM structure at an overall resolution of 3.6 Å (Figure 1D; Table S1), with resolution variation between 3.5 Å and 4.7 Å at 50 Å and 100 Å radial distance from the helical axis, respectively (Figure 1E). After density segmentation, we found that a single subunit has an elongated shape of 180 × 20 Å dimension, which is positioned perpendicularly to the rod axis (Figure 1F). When seen in top view, the subunit extends over one-third of the rod's cross section. In side view, the subunits are arranged like overlapping bricks that constitute the wall of the helical rod (Figure 1G).

PspA adopts an elongated four-helix core with an accessory C-terminal helix

Using the segmented density, we built an atomic model of a PspA monomer, covering residues 22–217 arranged in five α helices connected by loops (Figures 2A–2C). At one end of the elongated subunit, we identified a density that corresponds to the long α-helical hairpin PspA fragment (PDB: 4WHE) (Osadnik et al., 2015), independently confirming the chosen handedness of the cryo-EM map (Figure 2D). The best resolved density accommodates helices α1–α4 (25–185) (Figures 2E and 2F). We did not find density corresponding to a predicted N-terminal helix α0 (1–21) (Figure S1E), yet, we accommodated the amphipathic helix α5 (191–215) based on the weaker density attached to the outer wall of the helical rod (Figures 2G and S1F). Together, helices α1–α4 constitute the elongated four-helix core of the PspA molecules that form the wall of the tubular rod structure via a brick-like stacking. A total of 10.19 subunits are wound in a right-handed manner to form a single 360° turn with a pitch of 30 Å (Figure 2H). The top view of the assembly

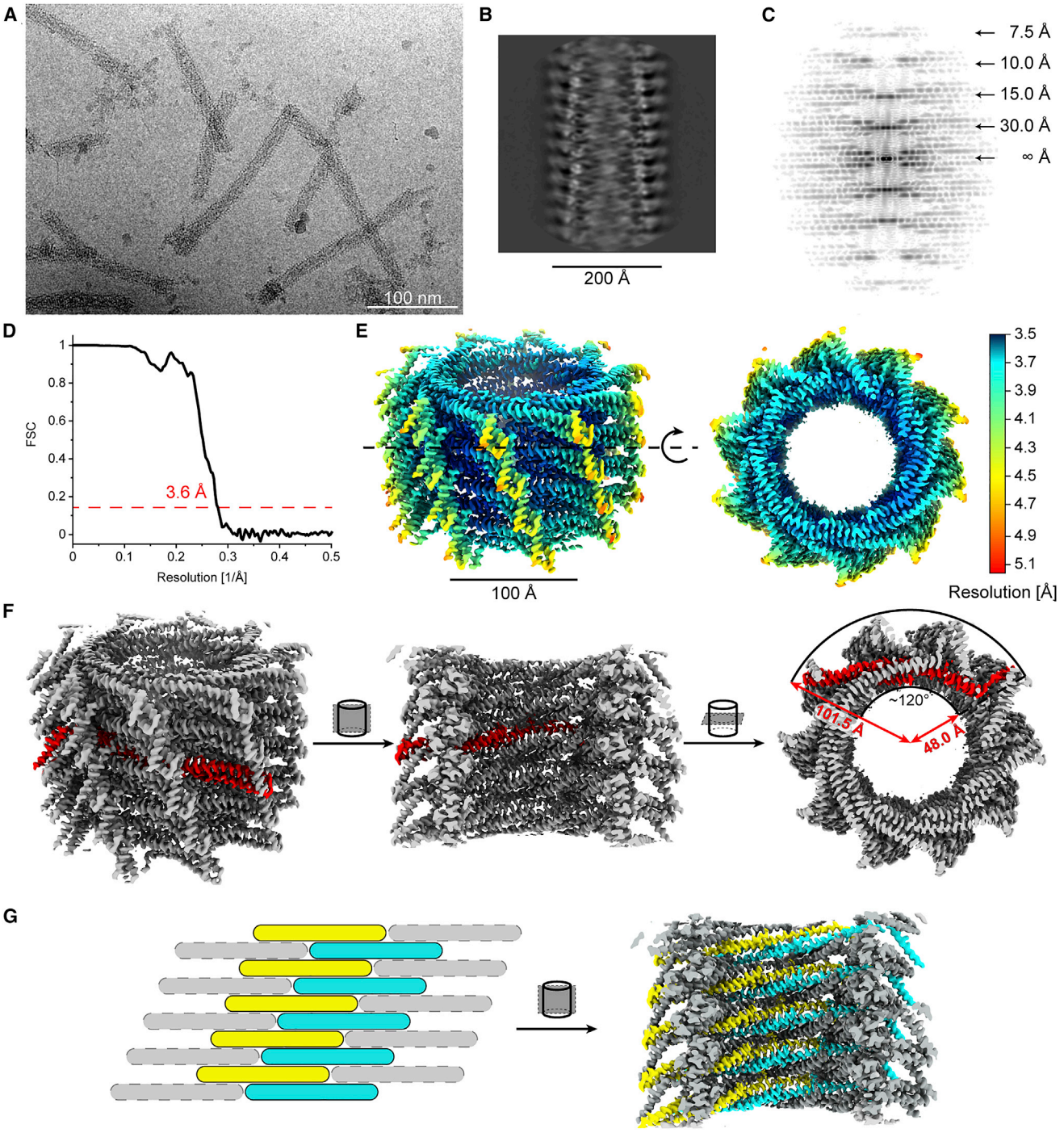

Figure 1. Cryo-EM structure of helical PspA assemblies

(A) Representative electron cryo-micrograph of PspA rods.

(B and C) (B) Detailed class average of Christmas-tree appearance and (C) corresponding power spectrum indicating layer lines up to 7 Å resolution.

(D) Fourier shell correlation supporting 3.6 Å resolution at the 0.143 cutoff.

(E) Local resolution estimates are mapped onto the surface of the PspA cryo-EM structure. The resolution varies from 3.5 Å at the inner wall to 4.7 Å at the C-terminal helix. See also Figures S1B–S1D and Table S1.

(F) Left: side view of cryo-EM density with a single segmented subunit in red. Center: open cylinder side view. Right: top view.

(G) Left: schematic view of subunits stacked like bricks forming a wall. Right: corresponding open half-cylinder view of stacked subunits forming the cylinder wall.

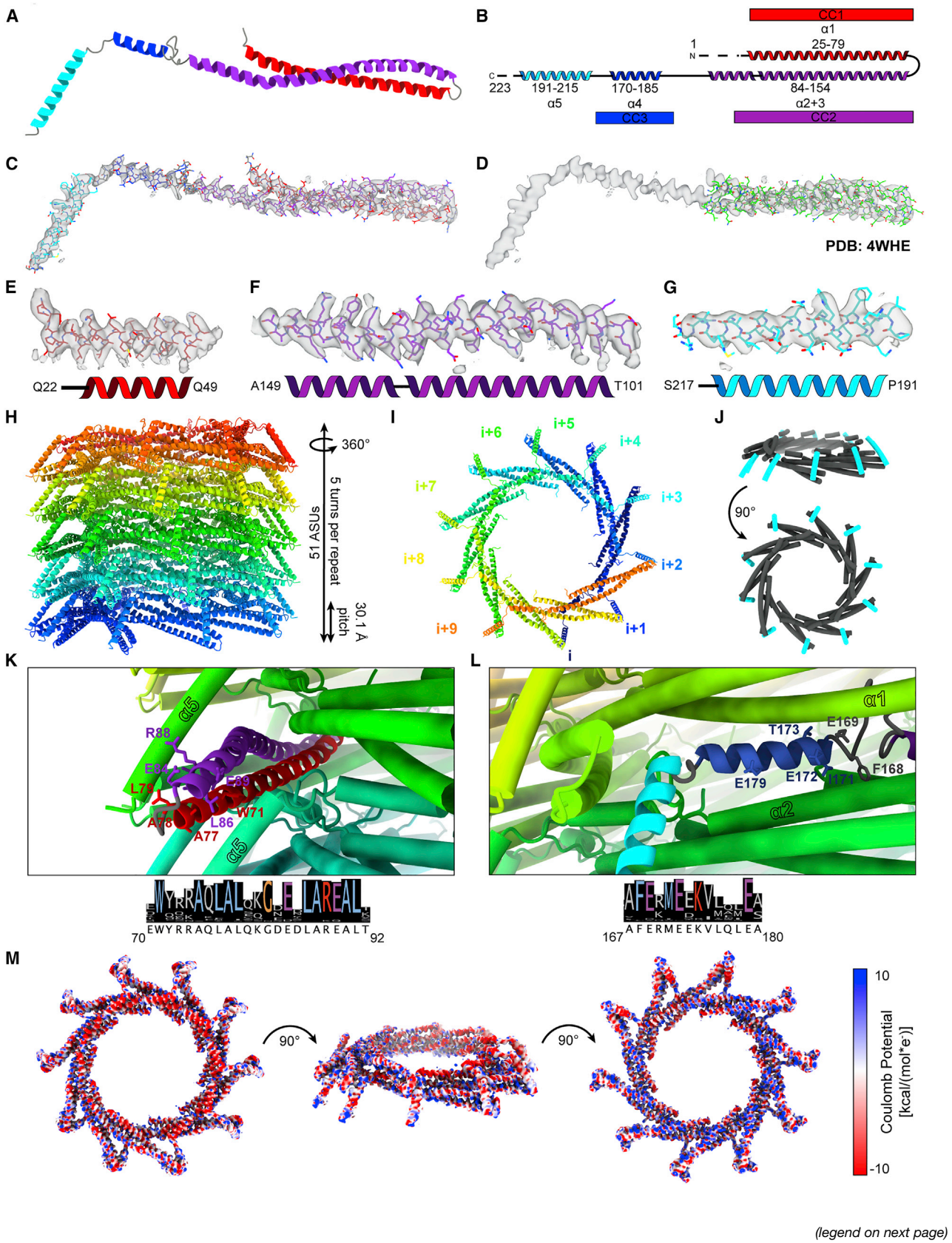

(legend on next page)

reveals that the PspA core helices are arranged like the diaphragm of an iris aperture pointing to the outside of the rod (Figure 2I), whereas the amphipathic paddle helix α5 at the C terminus emanates from the wall to the outside of the helical rod (Figure 2J). Interestingly, at both ends of the PspA core, first at the tip of the hairpin between helix α1 and α2 (70–90) and second at the opposite end of helix α4 (167–180), we find highly conserved (>90% identity) residues among the PspA/IM30 family of proteins (Figures 2K, 2L, and S1G) suggesting an evolutionary importance of these intersubunit stabilizing residues. Previously, mutation of these residues abolished formation of *Syn*IM30 rods, a closely related PspA homolog (Hennig et al., 2015; Saur et al., 2017). Therefore, we mutated the hydrophobic residues A75 and A78 and analyzed the PspA_A75S/A78S preparations using negative staining EM. Although PspA_A75S/A78S is still able to form rod structures, our image data suggest that mutant rods are less stable, in particular after refolding in the presence of 75 mM NaSCN when the mutant does not form rods anymore (Figures S2A and S2B). Moreover, we computed the Coulomb potential of the atomic model PspA assembly and found that both ends show opposite charges with a basic and acidic surface, respectively (Figure 2M), resulting in a polar assembly that has very different binding surfaces at each end of the assembly.

PspA shares the basic domain architecture with ESCRT-III proteins

Based on the determined cryo-EM structure of PspA, we found one particular structural feature (i.e., the helix α1/α2 hairpin packing against a perpendicular helix α5) reminiscent of previously resolved structures of eukaryotic membrane-remodeling ESCRT-III proteins. Therefore, we closely examined their apparent similarity by sequence alignment and compared cyanobacterial PspA and IM30 proteins with yeast Vps24 as well as human IST1 and CHMP1B (Figure 3), for which high-resolution cryo-EM structures have been determined. Interestingly, there are several stretches that show high sequence similarities (quality score >4) (Figure S2C). Furthermore, structural superposition of the α1/α2 hairpin region yields Cα root-mean-square deviations (RMSDs) with *Eco*PspA (PDB: 4WHE) (Osadnik et al., 2015), IST1 (PDB: 6TZA) (Nguyen et al., 2020), CHMP1B (PDB: 6TZ9) (Nguyen et al., 2020), and Vps24 (PDB: 6ZH3) (Huber et al., 2020) reporting average RMSD values of 1.6 Å, 2.3 Å, 2.2 Å, and 1.8 Å, respectively (Figure S2D). CHMP1B, Vps24, and PspA adopt elongated conformations, whereas IST1's structure was determined as a compact fold (Figure 4A). The corresponding resolved higher-order structures show that all of their assemblies remain unique (Figure 4B), whereas the fundamental organization of the α helices is conserved between all ESCRT-III proteins with helix-to-helix loops variations. Nevertheless, common to all structures is that the C-terminal helix α5 packs approx. perpendicularly against the α1/α2 hairpin motif (Figure 4C). Based on the identified structural similarities between the here-determined bacterial PspA cryo-EM structure and members of the eukaryotic ESCRT-III family, we conclude PspA may have shared evolutionary ancestry with ESCRT-III proteins.

PspA binds to lipid bilayers and converts small vesicles into large membrane structures

Due to the observed structural homology of PspA with ESCRT-III proteins, we tested whether PspA has a membrane remodeling activity in analogy to the ESCRT proteins. Therefore, we incubated preformed PspA rods with small unilamellar (SUVs) vesicles prepared from *E. coli* polar lipid extract (EPL) and analyzed the mixture using cryo-EM. In the cryo-micrographs of the PspA/EPL mixtures, PspA rods in solution as well as a large fraction of vesicles with increased diameters of >2 μm were observed. The large vesicles often have round and elongated shapes, enclose smaller deformed vesicles, and can even have more complex internalized lipid structures (Figures 5A, 5B, and S3A). As expected, in the SUV control, we visualized a population of small vesicles with 20–200 nm diameters (Figure 5C). Vesicle dimension and perimeter measurements indicate a significant increase of membrane length upon addition of PspA rods (Figures 5D–5F), suggesting the fusion of several smaller vesicles into one large vesicle. In many cases, the lipid bilayer appears to be interrupted by fuzzy stretches that have PspA protein density as well as PspA rods associated with the membrane (Figures 5B and S3B). Furthermore, when analyzing the membrane fine structure of large vesicles by 2D classification, the peak-to-peak separation of the bilayer increased from 3.0 to 5.4 nm on average when compared with the lipid samples alone (Figures S3C and S3D). Interestingly, the increased bilayer leaflet separation is only found in vesicles with perimeters larger than 175 nm, suggesting a post-fusion membrane structure induced by PspA. Additional micrographs of large unilamellar vesicles (LUVs) (Figure S4A) or the LUV/PspA mixture confirm the observation of an increased leaflet separation of 5.7 nm for fused

Figure 2. Atomic model and architecture of the helical PspA assembly

(A) Atomic model of PspA (22–217) with colored α helices in ribbon presentation (red, α1; purple, α2/α3; blue, α4; cyan, α5). See also Table S1.

(B) Secondary structure overlaid in the same color scheme as in (A) (see also Figure S1G) (helix nomenclature follows the ESCRT-III convention).

(C) Segmented cryo-EM density superimposed on built atomic model of PspA.

(D) Rigid body fit of the *Eco*PspA (25–141) X-ray structure (PDB: 4WHE).

(E–G) Density of helix α1 (E), helix α2/α3 (F), and helix α5 (G) at lower resolution.

(H) The rod assembly in side view: elongated monomers (in rainbow colors) assemble to form a right-handed helix of 10.19 subunits per turn (i.e., corresponding to a pitch of 30.1 Å).

(I) Top view of the assembly corresponding to one turn of stacked monomers i, i+1, i+2…i+9 (in rainbow colors).

(J) Helix α5 (cyan) forms a paddle that emanates from the wall to the outside of the helical rod.

(K and L) Scene 1 (residues 70–92) (K) and scene 2 (residues 167–180) (L) show the structural context of highly conserved side chains (color code as in B) in the PspA assembly (color code as in H).

(M) Electrostatic surface potential of PspA rods. The assembly consists of two unique ends with basic and acidic surfaces.

See also Figure S2.

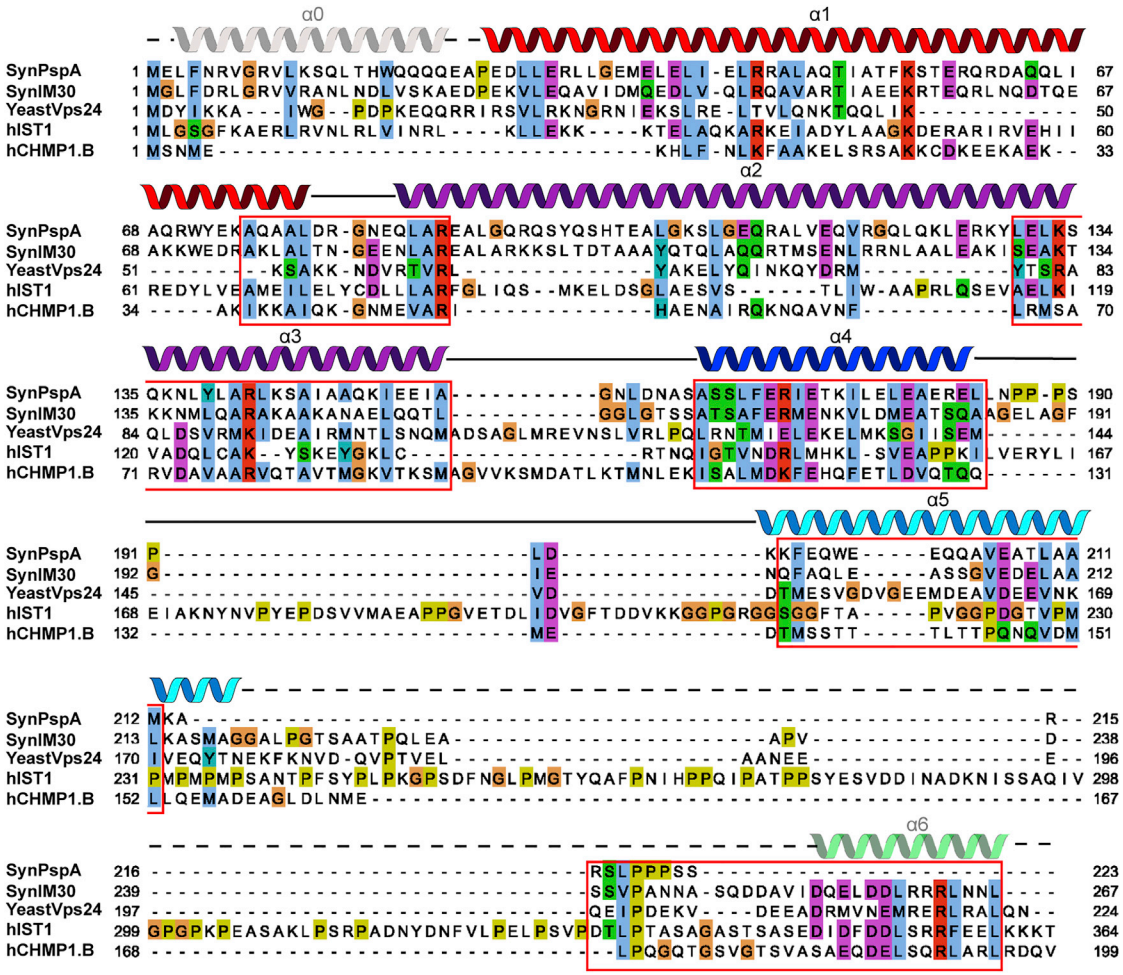

Figure 3. Sequence comparison of PspA/IM30 with ESCRT-III proteins

Sequence alignment of *Syn*PspA, *Syn*IM30, yeast Vps24, human IST1, and human CHMP1B superimposed with the secondary structures denoted by ESCRT-III nomenclature. Residues with similarity >30% are colored according to their properties (ClustalX color scheme). Stretches of high similarity are highlighted with red boxes. Alignment scores for the boxed areas are shown in Figure S2C. Sequences were aligned using the T-Coffee webserver (Di Tommaso et al., 2011) and visualized with JalView (Waterhouse et al., 2009).

See also Figure S2.

vesicles (Figures S4B and S4C). In fact, when we analyzed the interaction of PspA with model membranes using fluorescence spectroscopy, we observed binding of PspA to negatively charged PG-containing membranes (Figure 5G), as well as net uncharged PC membranes (Figures S5A and S5B). Destabilized rods (PspA_A75S/A78S) also bound to model membranes, even with higher apparent affinity, supporting the observation that PspA membrane binding involves rod disassembly.

Next, we inspected a large dataset of 1,531 cryo-EM images of PspA rod structures in the presence of EPL SUVs in more detail (Figure S5C). Based on 2D classification, 65% of rods show a diameter of 275 Å, whereas only 35% share the narrower diameter at 220 Å observed in the PspA alone rod sample (Figures S5D and S5E). The wider rods (from here: PspA+EPL rods) show a different power spectrum as they form a two-start helix with 13.52 subunits per turn and a pitch of 59.9 Å (Figure S5F). Using these helical symmetry parameters, we determined a 7.2 Å cryo-EM density of PspA+EPL rods, which we could fit by the built atomic model of PspA (Figures 5H and S5G–S5I). Notably, PspA+EPL rods enclose a density of lower but significant density forming a separate inner cylinder of ~40 Å thickness. Interestingly, the cryo-EM structure of PspA alone having a smaller diameter also has a pronounced inner density (Figures S5J and S5K), which we attribute to co-purified residual lipids. In addition, we observed a small tubular stalk that protrudes from helix α1 of strand B into the rod lumen (Figure 5I), which we interpreted as density for helix α0. Overall, the conformation of PspA determined from PspA+EPL and PspA rods share the same ESCRT-III fold (Figures S5L and S5M). The increased width of PspA+EPL rods is compatible with a lipid bilayer present in the inner lumen, which can also be observed in image slices of tomograms of PspA+EPL rods (Figure S6A). The experiments with preformed PspA rods and EPL show that the observed vesicle growth is consistent with a membrane

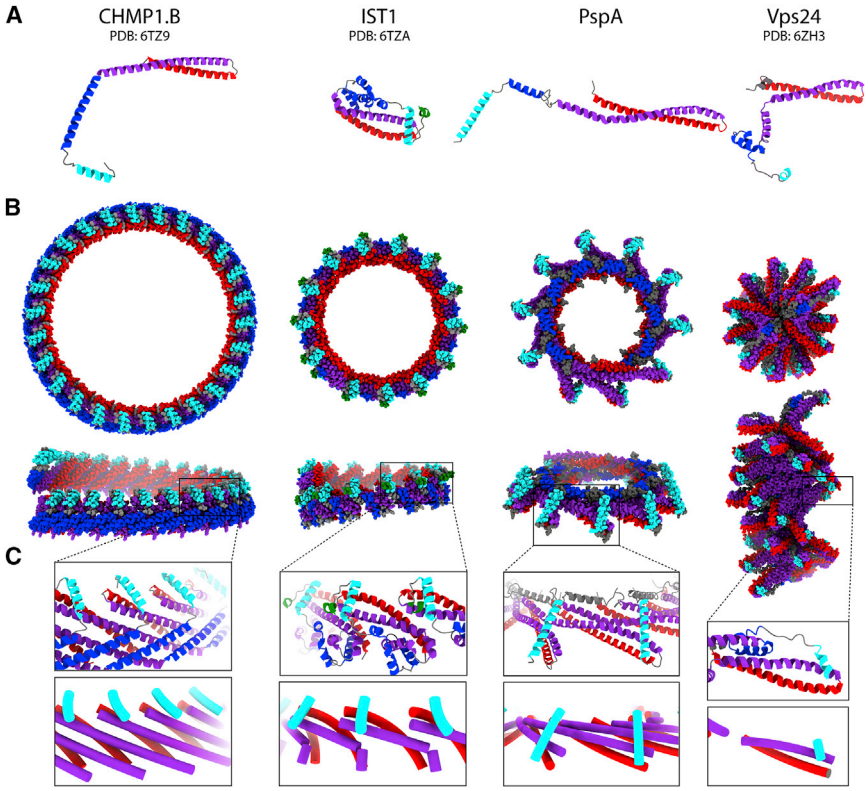

Figure 4. Comparison of PspA and ESCRT-III structures

(A) Views of CHMP1B, IST1, PspA and Vps24 monomers with colored α helices in ribbon presentation (red, α1; purple, α2/α3; blue, α4; cyan, α5).

(B) Helical assemblies of ESCRT-III proteins and PspA in sphere representation (color code as in A). Upper row: top views. Lower row: side views.

(C) Details of the ESCRT-III and PspA assemblies showing a conserved motif with helix α5 being packed approximately perpendicularly against the α1/α2 hairpin motif.

remodeling activity, and wider rod structures can potentially accommodate a lipid bilayer in the lumen of the helical rod.

PspA rods can enclose lipid bilayers and give rise to internalized membrane structures

To study the effect of assembling PspA monomers on liposome membranes rather than preformed PspA rods, we designed a cleavage-inducible assembly variant of PspA (CIA-PspA) that is impaired in rod assembly due to the presence of a N-terminal NusA-tag (Figure 6A, left). When releasing the NusA-tag from PspA upon 3C protease cleavage, PspA monomers assemble into PspA rods. We found that CIA-PspA remodels liposomes into membrane tubules (Figure 6A, right) and observed μm-sized clusters of small and large deformed vesicles as well as PspA rods emanating from vesicles (Figures 6B, S6B, and S6C). In analogy to the incubation with preformed PspA rods, we also observed a pronounced modification in bilayer leaflet separation up to 4.0 nm (Figure S3D, right). Cryo-tomographic slices (Figure 6C) of approximately 50% of CIA-PspA rods show clear tubular lipid bilayer density protruding from the vesicle into the lumen of the rods, whereas other smaller diameter CIA-PspA rods did not enclose tubular lipid bilayers (Figure S6D). Interestingly, the rods were always attached to small vesicles with a consistent polarity with respect to the vesicles. By superimposing the PspA+EPL rods with CIA-PspA rods in the tomographic slices, we infer that the rods attach to the vesicles with their negatively charged end (Figures 6C and S5N). In conclusion, PspA rods can incorporate a lipid bilayer into the central lumen producing constricted positively curved membrane tubules.

However, mixtures of PspA and EPL SUVs have a broad distribution of vesicle sizes and membrane structures. In-depth analysis of a representative tomogram by continuous z slices reveals that multiple vesicles are often connected, thus forming an intricate system of membranous cisternae linked together by proteinaceous high-density zones (HDZ), where distinct lipid bilayer density is absent (Figure 6D; Video S1) giving rise to the observed fuzzy stretches in the 2D images described above. Nevertheless, HDZs can often be found close to areas of high lipid curvature at the cone-shaped and tubule-like ends of pear-shaped vesicles (Figures 6E and 6F). Close to HDZs, often internalized vesicles can be found connected to a larger vesicle suggesting an internal budding process (Figure 6G). Together with the observed structural ESCRT-III homology, co-reconstitution with lipids demonstrates that PspA is capable of mediating vesicle growth as well as membrane constriction and fission in dependence on the initial oligomeric state, and can, therefore, be considered a bona fide member of the ESCRT-III family of membrane remodeling proteins.

DISCUSSION

The propensity of PspA to form higher-order structures has been shown early on (Hankamer et al., 2004; Kobayashi et al., 2007), yet how oligomerizations contributes to the basic physiological PspA function of maintaining membrane integrity remained uncertain. Here, we determined the 3.6 Å resolution cryo-EM structure of PspA rod assemblies and systematically studied the interaction of PspA with membranes. Due to similar structural and functional properties of PspA and eukaryotic ESCRT proteins, we identified PspA as a bacterial member of the evolutionary conserved ESCRT-III superfamily of membrane remodeling proteins.

Although EcoPspA forms rings rather than rods (Hankamer et al., 2004; Kobayashi et al., 2007), the physiological importance of ring versus rod structures remains an open question, because these structures have not been observed in their native context yet. Structurally, rods and rings are closely related, and conversion can be easily envisioned by accommodating small angular changes in subunit-subunit interactions. Using *in vivo*

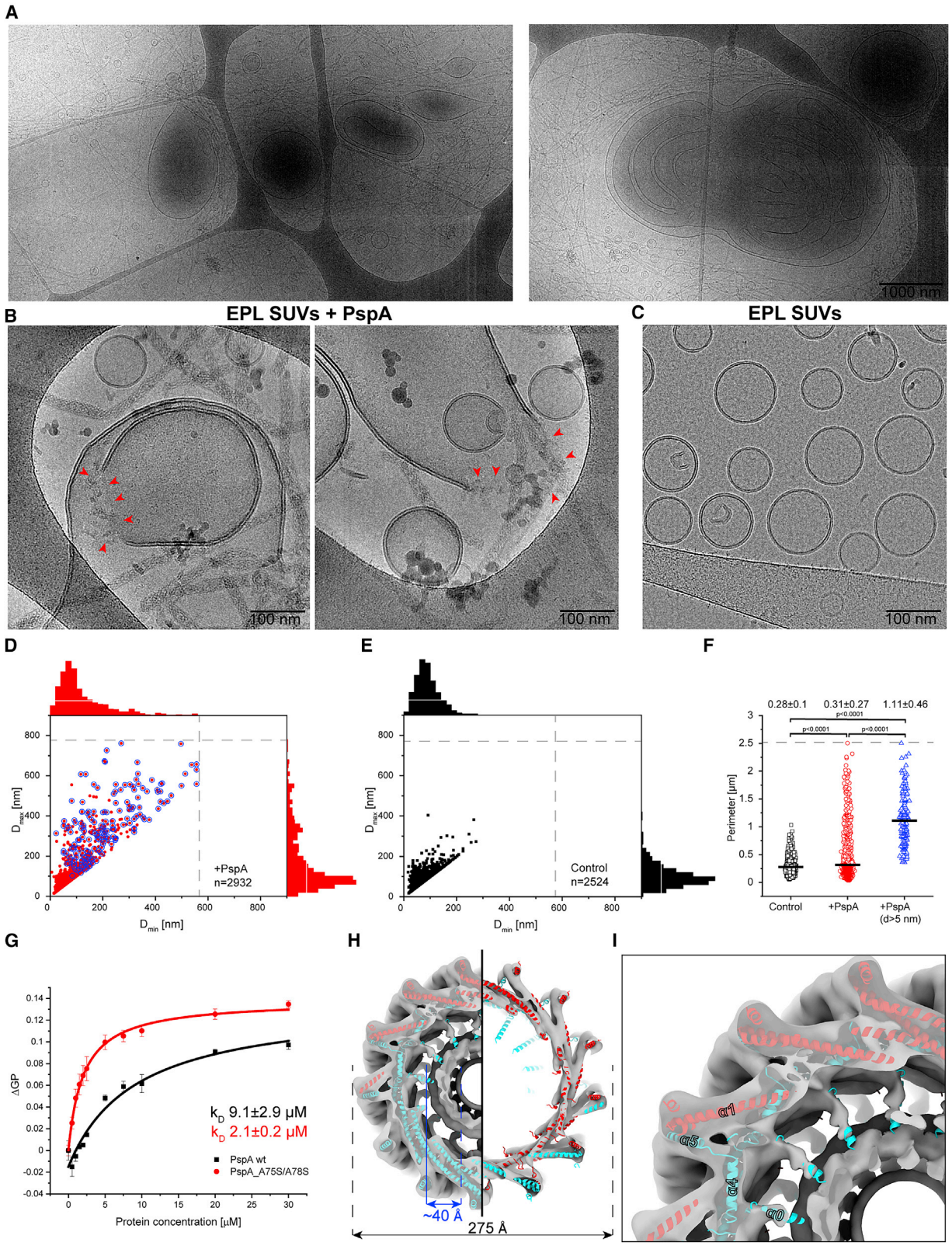

(legend on next page)

fluorescence microscopy, IM30 and PspA were shown to form dynamic localized *puncta* in *Synechocystis* and *E. coli* (Engl et al., 2009; Gutu et al., 2018; Jovanovic et al., 2014; Yamaguchi et al., 2013), which is consistent with formation of rings, transient rod, or other higher-order structures associated with cellular membranes (Junglas and Schneider, 2018; Siebenaller et al., 2019). We and others (Engl et al., 2009) observed that such PspA assemblies were preferentially found at the cell poles, most likely to protect vulnerable cell membrane regions from dissipation of the proton motive force.

Due to revelation of PspA as a member of an ESCRT-III superfamily, we wondered whether there are more structural similarities beyond the identified homology and fold. Purified ESCRT-III proteins are known to assemble into a variety of large EM-observable structures, among them strings, rings, coils, sheets, filaments, and domes (Bodon et al., 2011; Ghazi-Tabatabai et al., 2008; Lata et al., 2008). Due to the large number of isoforms of eukaryotic ESCRT-III proteins, the complexity of assembling hetero-complexes is significantly increased, and multiple combinations have been investigated (Henne et al., 2011; Huber et al., 2020; Pfitzner et al., 2020). A structural motif of striking similarity found in PspA as well as in eukaryotic ESCRT structures is the perpendicular packing of helix α5 against the α1/α2 hairpin (Figure 4). Additionally, helix α4 establishes important intersubunit contacts in the central core of the polymers, which is reflected in a stretch of residues with properties conserved between PspA/IM30 and ESCRT III proteins (Figure 3). Although the AAA-ATPases PspF and Vps4 disassemble *Eco*PspA or eukaryotic ESCRTs, respectively, PspF is not encoded in *Synechocystis*, and other PspA-interacting ATPases have not been identified. Yet, a currently enigmatic ATPase may be involved in regulating the PspA activity in *Synechocystis* given the central importance of Vps4 in the ESCRT-III membrane remodeling pathway.

Despite the matching structural organization of PspA and ESCRT-III proteins, we further assessed whether PspA and ESCRT-III proteins have functional similarities. Consistent with the function of ESCRT-III being involved in membrane remodeling processes, PspA co-incubated with EPL revealed two noteworthy details: PspA binding to membrane surfaces induced a leaflet separation >5 nm and the appearance of remodeled liposomes. Observations include PspA-mediated vesicle growth as well as formation of membrane tubules and internalized membrane structures resulting from fusion, constriction, and fission events. The widening of the lipid bilayer likely is a consequence of PspA rod disassembly and the formation of a PspA carpet on the membrane surface, as recently described for IM30 (Junglas et al., 2020). As observed here, membrane adhesion and partial incorporation of PspA molecules into the membrane will lead to the thickening of the lipid bilayer. The observed bilayer structures could represent a protected form of the lipid bilayer minimizing, for instance, leakage of protons under imposed membrane stress conditions (Junglas et al., 2020; Kobayashi et al., 2007). Electrostatic surface analysis of the PspA rod structure reveals an acidic and a basic end, which could provide a rationale for PspA's observed preference of binding to negatively charged membrane surfaces (Kobayashi et al., 2007; McDonald et al., 2015, 2017). Yet, our membrane interaction studies show that PspA is also capable of binding to net uncharged membrane surfaces, and, therefore, membrane interaction of PspA appears to be less charge-dependent than observed for *Syn*IM30 (Hennig et al., 2015).

The imaged liposomes also show high-density zones devoid of any visible organized lipid bilayer structure, often with PspA rods attached to the vesicle surface. The corresponding regions contain a grainy texture suggestive of floating PspA molecules dissociated from the rod into smaller units. Because they make up the linkages of a continuous vesicular lipid network, they likely constitute lipid transfer zones (LTZs), enabling lipid movement between vesicles. In this role, LTZs may locally replace the bilayer structure while giving up the characteristic phospholipid barrier structure. In many aspects, the LTZs observed here and PspA's membrane activity are reminiscent of the detergent-like membrane interaction of linear amphipathic antimicrobial peptides (for review, see Bechinger and Lohner, 2006). In previous experiments, it has been observed that interaction of *Syn*IM30 with membranes disturbs the bilayer structure and allows small molecules to enter liposomes (Hennig et al., 2015), and an antimicrobial peptide-like activity has been discussed (Thurotte and Schneider, 2019). Importantly, a detergent-like behavior of PspA does not exclude formation of stabilizing membrane carpets and formation of destabilizing pore-like structures within a membrane.

Figure 5. Membrane binding and remodeling by PspA

(A) Electron cryo-microscopy (cryo-EM) overview images of small unilamellar vesicles (SUVs) prepared from *E. coli* polar lipid extract (EPL) incubated with PspA rods.

(B and C) High magnification cryo-EM images of EPL SUVs incubated with PspA rods and EPL SUVs alone, respectively. Fuzzy stretches devoid of a continuous lipid bilayer are marked by arrowheads.

(D and E) Scatterplots of EPL vesicle dimensions in the presence of PspA rods and EPL SUVs alone, respectively (gray dashed line represents micrograph field of view). Stacked histogram charts on the right and top axis. (E) EPL forms small uniform vesicles in the absence of PspA, whereas (D) larger deformed vesicles are often observed with a bilayer leaflet separation >5 nm (blue circles). A representative gallery of diverse EPL vesicles after incubation with PspA rods is shown in Figure S3.

(F) Statistical analysis of the vesicle perimeters of EPL SUVs control (black) and after incubation with PspA rods (red) and a subset of vesicles with $d > 5$ nm (blue) (errors represent SD, n = 2,524 [black], 2,932 [red], and 176 [blue]).

(G) Membrane binding of PspA wild-type (black) and A75S/A78S (red) to negatively charged membranes (40%PG/60%PC) was analyzed by monitoring changes in the Laurdan GP values upon addition of increasing PspA concentrations (error bars represent SE, n = 3). The A75S/A78S mutant giving rise to destabilized rods binds with higher apparent affinity to membrane surfaces. See Figures S5A and S5B for the full Laurdan fluorescence spectra.

(H and I) Cryo-EM density of PspA+EPL rods superimposed with helical assembly (red, strand A; cyan, strand B) at 7.2 Å resolution. The rods have a width of 275 Å including an inner lumen cylinder density with a thickness of ~40 Å. The inner density is connected to the rod assembly wall by a small tubular stalk that was interpreted as helix α0.

See also Figure S4 and Table S1.

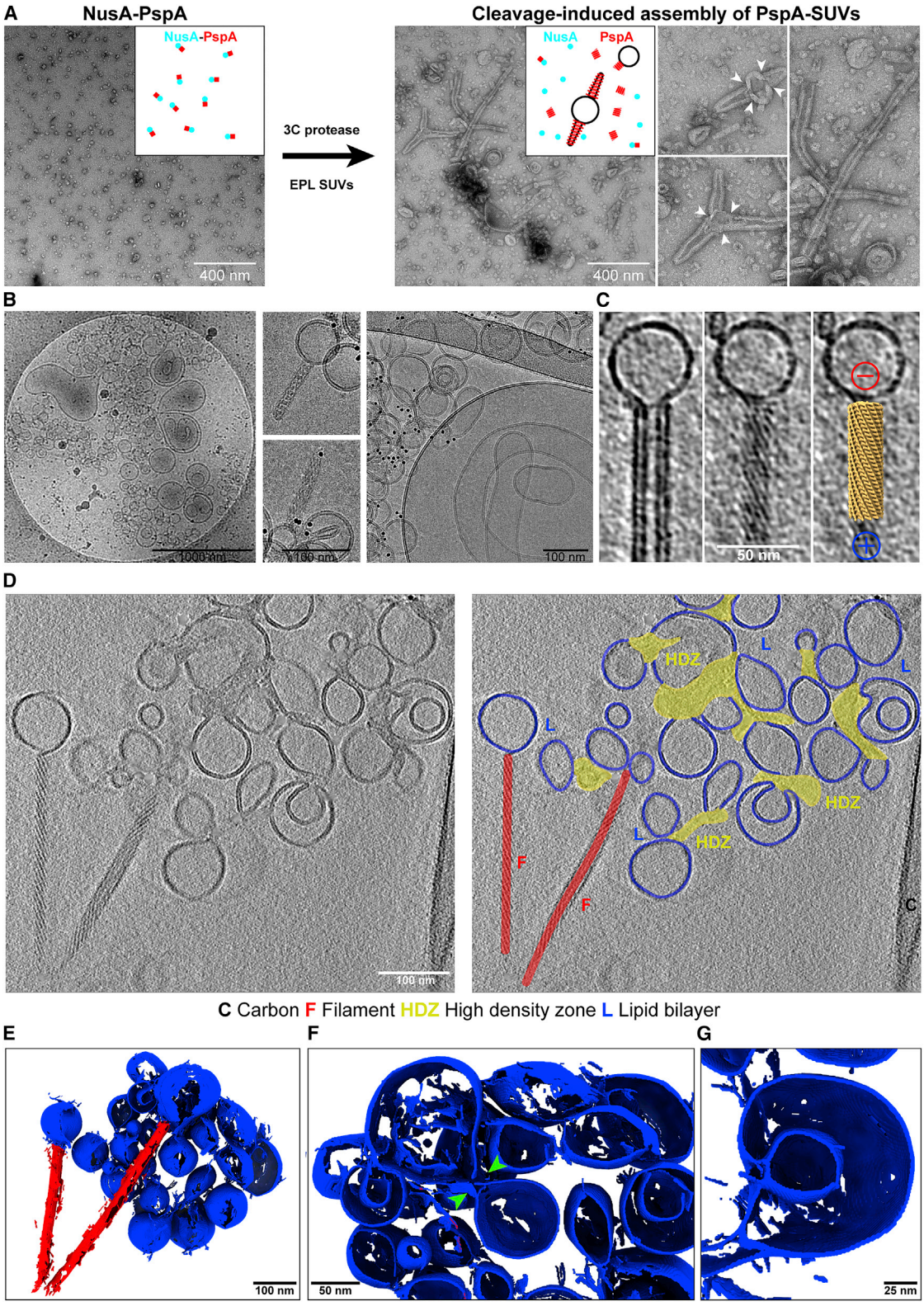

Figure 6. Structures of membrane-attached PspA rods formed by cleavage-induced assembly (CIA-PspA)

(A) Negatively stained electron micrographs of NusA-PspA and CIA-PspA. After 3C protease addition to NusA-PspA (globular structures) in the presence of EPL SUVs, PspA spontaneously forms membrane tubules attached to vesicles (white arrowheads point to tubule-vesicle contact sites).

(legend continued on next page)

The cryo-EM structures of PspA and PspA+EPL rods determined here bear the most apparent similarity with the determined IST1/CHMP1B ESCRT-III assembly (McCullough et al., 2015). More recently, IST1/CHMP1B could also be reconstituted with negatively charged lipids that were found in the lumen of the assembly (Nguyen et al., 2020). In the presence of lipids, the diameter of the IST1/CHMP1B tubular assemblies increased from 240 to 280 Å leading to the hypothesis of high and low constriction states, respectively. In analogy to the IST1/CHMP1B as well as *Chlamydomonas* IM30/Vipp1 rods (Theis et al., 2019), we observed that PspA rods can include lipid bilayers in the lumen, accompanied by changes in diameter from 220 to 275 Å, which therefore represent different constriction states. It is noteworthy that our preparations of PspA alone also revealed a significant variation of the diameters of the rods. This structural flexibility may be an important property of PspA to accommodate different bilayer intermediate configurations during the lipid interaction process. Furthermore, in the presence of lipids, we detected density for helix α0 in the PspA rod structure consistent with folding of N-terminal helix peptides of PspA and IM30 in the presence of lipid bilayers (McDonald et al., 2015, 2017). Taken together, PspA rods are strong candidates for membrane remodeling proteins generating positive curvature, because IST1/CHMP1B and PspA assemblies share the same principal rod architecture, lipid topology, and changes in diameters.

In order to describe the biogenesis of the observed membrane fusion, constriction, and fission activities, we sorted the set of recorded membrane events to enable interpretation in a sequential manner. Initially, PspA assembles in rods free in solution or starting from a membrane anchored platform (Figure 7, top). The PspA+EPL intermediate resolution cryo-EM structure and cryotomograms show that these membrane-attached rods incorporate lipid bilayer tubules into the observed wider structures. The polar rods grow at the positively charged ends at the tip until they may encounter other free vesicles containing negatively charged lipids. In this contact area, ordered PspA rods start to disassemble at their positive end and initiate formation of LTZs, connecting two vesicular structures (Figure 7, center). After this docking event, the vesicular lobes form the structure resembling an hourglass linked by the PspA LTZ. This hourglass structure likely represents a critical switch structure that we propose can undergo two principal pathways: in the first case, lipid movement is allowed over the LTZ and the donor membrane of vesicle 1 is in close spatial proximity to the acceptor membrane of vesicle 2. Then, lipid transfer across a newly formed continuous lipid structure can take place thereby fusing the bilayers of vesicle 1 and 2. Upon relaxation of the lipid bilayer structure, larger vesicles consisting of the fused membranes of vesicle 1 and 2 have formed (Figure 7, bottom left). In the second case, lipid movement is allowed over the LTZ and the donor membrane of vesicle 1 is not in closest spatial proximity to the membrane of vesicle 2. Here, the membranes of vesicles 1 and 2 do not form a continuous bilayer, and as a result, the membrane of vesicle 1 buds into the lumen of vesicle 2, resulting in two separate membrane systems. In consequence, a cross-membrane transfer of vesicle 1 into the lumen of vesicle 2 and membrane fission is observed (Figure 7, bottom right), reminiscent of ESCRT-III inward vesicle budding events. We would like to point out that in our *in vitro* reconstituted samples, we classified these two principal cases, although we also observed multiple intermediate events and combinations of these two outlined pathways (e.g., including a symmetric cross-membrane vesicle transfer and multiple others) (Figure S7). According to this fusion-fission switch model, the critical step that determines the fate of fusion or fission may be the spatial proximity of the donor and acceptor membrane that enables or disables the formation of a continuous lipid bilayer. In both of the described activities, PspA's mode of action results from the ability to move lipids across the LTZ.

The fusion-fission switch model described here explains a multitude of the observed membrane activities of PspA. Upon occurrence of membrane leakage, PspA-induced vesicle growth can potentially patch disturbed membranes and restore full membrane integrity thereby protecting bacterial membranes, because it has been hypothesized previously for the bacterial dynamin-like protein DynA after treatment of membranes with pore-forming agents (Guo and Bramkamp, 2019). In addition to this active repair mechanism, PspA likely is also capable of passive membrane protection by forming a protective carpet on membranes, as described above. Furthermore, PspA-induced cross-membrane vesicle transfer can result in the formation of intricate internalized membrane systems reminiscent of thylakoid membrane stacks that are known to be mediated by the PspA homolog IM30 (Heidrich et al., 2017; Vothknecht et al., 2012). Similarly, inward vesicle budding, as it has been attributed to eukaryotic ESCRT-III action during multivesicular body biogenesis, could also be envisioned by the process of cross-membrane vesicle transfer. In case PspA's mode of action was transferable to eukaryotic ESCRT-III proteins, the determined structure of IST1/CHMP1B polymer would be directly compatible, because it has also been shown to bind lipids in the lumen of the assembly. In contrast to lipid reconstitutions mediated by several eukaryotic ESCRT proteins, the homo-oligomer of PspA alone induces large-scale changes to liposome morphology, including growth, constriction, and cross-membrane vesicle transfer. Thereby, it represents a minimal bacterial membrane remodeling system that is capable of triggering membrane fusion and fission *in vitro*.

(B) Cryo-EM micrographs of CIA-PspA in presence of EPL SUVs. Left: overview image indicates structural diversity of vesicles in this sample (see also Figure S6). Center and right: detailed images of rods attached to vesicles and fused or deformed vesicles.
(C) Tomogram slices of a CIA-PspA rod attached to a vesicle. Left: central slice showing a lipid bilayer in the inner lumen. Center: top slice showing striations of the outer helical lattice. Right: top slice superimposed with a model of the polar PspA+EPL rod. The negatively charged end of the rod faces the vesicle.
(D) Left: representative cryo-electron tomogram of CIA-PspA and a cluster of EPL SUVs (Video S1). Right: the same tomogram with superimposed 2D segmentation showing rods in red, high-density zones (HDZ) in yellow and lipid bilayers in blue.
(E) 3D segmentation of the tomogram shown in (D). The vesicles and HDZs form an interconnected 3D lipid/PspA network.
(F) Zoomed view of the interconnected lipid/PspA network with two fusing vesicles (green arrow heads) in the center.
(G) Detailed view of a larger vesicle with an enclosed budding vesicle.

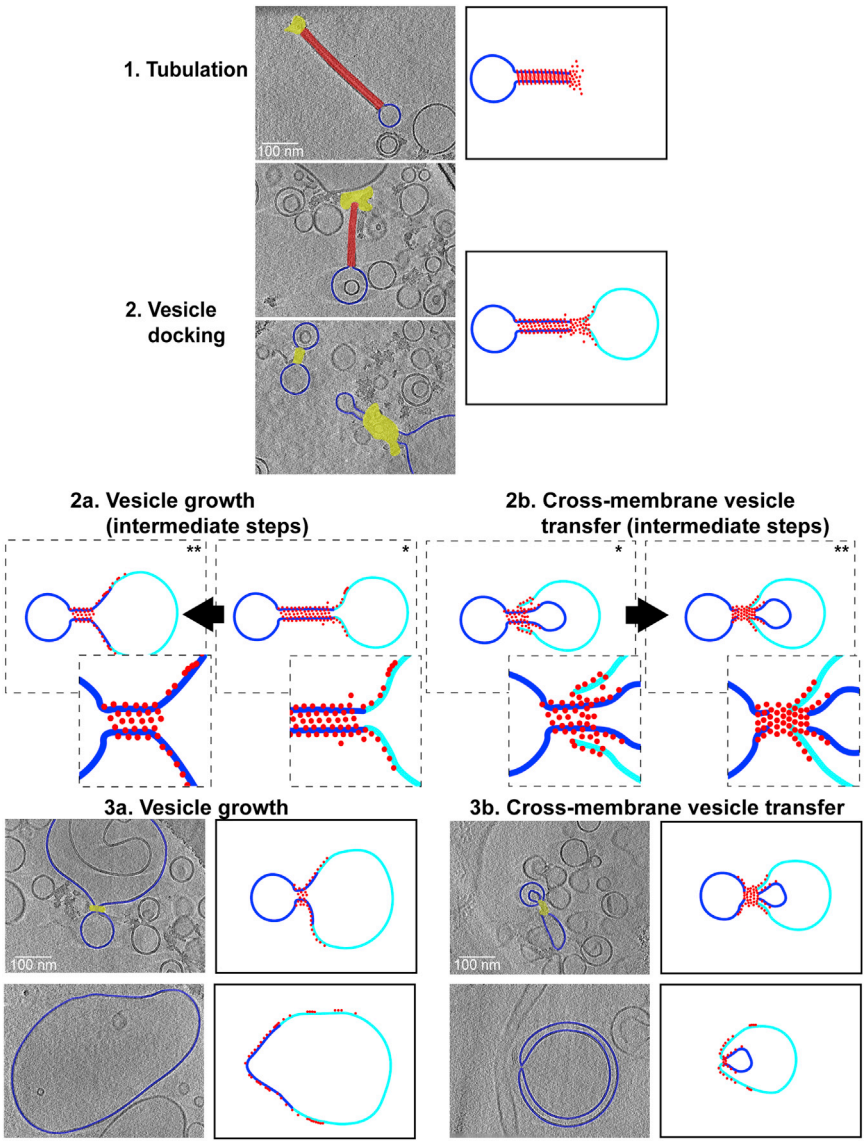

Figure 7. Model of PspA membrane remodeling activity resulting in vesicle growth and cross-membrane vesicle transfer

A potential sequence of events leading to vesicle growth and cross-membrane vesicle transfer supported by cryo-EM images. Left column: cryo-electron tomograms of PspA interacting with vesicles superimposed with 2D segmentation of the region of interest (rods in red, lipid transfer zones in yellow and lipid bilayers in blue). Corresponding non-segmented tomogram slices shown in Figure S7. Right column: simplified model (blue, donor membrane; cyan, acceptor membrane; red, PspA). The initial two steps are identical for vesicle growth and cross-membrane vesicle transfer: (1) tubulation, PspA assembles into rod structures anchored with one vesicle in a polar manner. (2) Vesicle docking, a second vesicle will be contacted by the PspA rod linking the two vesicles. Switch point leading either to (2a) or (2b) that represent proposed intermediate steps (dashed box with zoomed insets of lipid transfer zones): depending on the spatial proximity of the donor and acceptor membrane within the lipid transfer zone (3a) vesicle growth or (3b) cross-membrane vesicle transfer can occur. Relaxation of vesicular constriction leads to a large fused vesicle. Donation of lipid vesicle into lumen of juxtaposed vesicle leads to an internalized membrane structure.

Limitations of the study

This study establishes that PspA is a member of the membrane remodeling ESCRT-III protein family. In support, this membership has just now been confirmed for PspA-related bacterial IM30/Vipp1 proteins by two independent studies: first, derived from bioinformatic analysis and followed by single-particle cryo-EM of IM30/Vipp1 rings revealed a conserved ESCRT-III fold (Liu et al., 2021 [this issue of *Cell*]). Second, the cryo-EM single-particle structure of IM30/Vipp1 rings as well as *in situ* cryo-EM studies revealed the presence of Vipp1 rods in *Chlamydomonas reinhardtii* (Gupta et al., 2021 [this issue of *Cell*]). These studies also show the structural diversity, because IM30/Vipp1 forms rings in cyanobacteria, whereas cyanobacterial PspA and IM30/Vipp1 of *Chlamydomonas reinhardtii* form rods. The physiological impact and consequences of rings versus rods are currently still open questions. Based on cryo-electron tomography analyses, using PspA reconstituted with membranes, we here propose a sequence of events leading to either membrane fusion or fission. However, this sequence was not directly determined by our cryo-EM experiment. Instead, the model was derived from images that were assembled in a sequence, showing the recorded structures as putative stages of a continuous membrane remodeling process. Short-lived intermediates, however, are notoriously difficult to capture by cryo-EM and, therefore, could be missing in our model. In addition, the PspA rod structures determined here do not allow the detailed description of the molecular mechanism of membrane remodeling. When lipid tubule density was present in the PspA EPL structure, helix α0 was detectable, yet the exact conformations of the lipid-interacting residues remain open at the given resolution. The prominent role of the helix α1/α2 hairpin (α2/α3 in IM30 nomenclature) in membrane fusion or fission, as identified analyzing the closely related *Synechocystis* IM30/Vipp1 (Thurotte and Schneider, 2019), could not be directly visualized or clarified here. Moreover, how PspA interaction gives rise to the increased bilayer thickness in the observed post-fusion membranes remains unclear. Better resolution of these intermediate structures could reveal the exact paths leading to fusion or fission and may even clarify how the PspA membrane remodeling machinery also accomplishes the different roles of membrane protection *in vivo* (Kleerebezem et al., 1996; Kobayashi et al., 1998, 2007).

Our study reveals many functional details on PspA's membrane remodeling activities based on cryo-EM structures, while it also raises a series of new questions on the functional relationship between bacterial PspA/IM30/LiaH and the eukaryotic ESCRT-III proteins: are the observed PspA's remodeling activities fully transferable to the diversity of activities of eukaryotic ESCRT-III proteins? Do even the prokaryotic IM30 or LiaH share the same mechanisms of membrane remodeling? Do, in analogy to eukaryotic ESCRT-III, regulators exist *in vivo* that direct PspA's membrane remodeling activities to fulfill different functions in membrane organization, repair, and maintenance? To address these open questions, it will be important to conduct further mechanistic studies, including structural work, to develop a more general framework for the membrane remodeling activity of the ESCRT-III protein family as a whole.

STAR★METHODS

Detailed methods are provided in the online version of this paper and include the following:

- KEY RESOURCES TABLE
- RESOURCE AVAILABILITY
  - Lead contact
  - Materials availability
  - Data and code availability
- EXPERIMENTAL MODEL AND SUBJECT DETAILS
  - Bacterial cells
- METHOD DETAILS
  - Expression and purification of PspA
  - Lipid reconstitution
  - Membrane binding assay
  - Cleavage-induced assembly of PspA rods (CIA-PspA)
  - Fluorescence microscopy
  - Negative staining electron microscopy
  - Electron cryo-microscopy
  - Electron cryo-tomography (cryo-ET)
  - Image processing and helical reconstruction
  - Cryo-EM map interpretation and model building
  - Cryo-ET image processing
  - Image analysis of membranes
- QUANTIFICATION AND STATISTICAL ANALYSIS

SUPPLEMENTAL INFORMATION

Supplemental information can be found online at https://doi.org/10.1016/j.cell.2021.05.042.

ACKNOWLEDGMENTS

We acknowledge support with microscope operation, image acquisition, and preparation of Figure 6 by Julio Ortiz in addition to helpful discussions. The authors gratefully acknowledge the computing time granted through JARA on the supercomputer JURECA at Forschungszentrum Jülich (Krause, 2019). This work was funded by the Max-Planck Graduate Center at the Max Planck Institutes and the University of Mainz. This work has been initially supported by iNEXT (653706) funded by the Horizon 2020 program of the European Union.

AUTHOR CONTRIBUTIONS

B.J., D.S., and C.S. designed research. B.J. and L.S. purified the proteins. B.J., T.H., and M.C. prepared cryo-EM samples. T.H., M.C., and B.J. operated the electron microscopes. B.J. and S.T.H. determined the cryo-EM structures. D.M. and B.J. built the refined atomic model. R.H. performed mutation experiments. B.J. and N.H. performed membrane-binding experiments. L.S. conducted the *in vivo* experiments and fluorescence microscopy. B.J., D.S., and C.S. wrote the manuscript with input from all authors.

DECLARATION OF INTERESTS

The authors declare no competing interests.

Received: September 16, 2020
Revised: March 1, 2021
Accepted: May 26, 2021
Published: June 23, 2021

REFERENCES

Afonine, P.V., Klaholz, B.P., Moriarty, N.W., Poon, B.K., Sobolev, O.V., Terwilliger, T.C., Adams, P.D., and Urzhumtsev, A. (2018). New tools for the analysis and validation of cryo-EM maps and atomic models. Acta Crystallogr. D Struct. Biol. *74*, 814–840.

Afonine, P.V., Poon, B.K., Read, R.J., Sobolev, O.V., Terwilliger, T.C., Urzhumtsev, A., and Adams, P.D. (2018). Real-space refinement in PHENIX for cryo-EM and crystallography. Acta Crystallogr. D Struct. Biol. *74*, 531–544.

Ashkenazy, H., Abadi, S., Martz, E., Chay, O., Mayrose, I., Pupko, T., and Ben-Tal, N. (2016). ConSurf 2016: an improved methodology to estimate and visualize evolutionary conservation in macromolecules. Nucleic Acids Res. *44* (W1), W344-50.

Baba, T., Ara, T., Hasegawa, M., Takai, Y., Okumura, Y., Baba, M., Datsenko, K.A., Tomita, M., Wanner, B.L., and Mori, H. (2006). Construction of Escherichia coli K-12 in-frame, single-gene knockout mutants: the Keio collection. Mol. Syst. Biol. *2*, 2006.0008.

Bechinger, B., and Lohner, K. (2006). Detergent-like actions of linear amphipathic cationic antimicrobial peptides. Biochim. Biophys. Acta *1758*, 1529–1539.

Beckers, M., and Sachse, C. (2020). Permutation testing of Fourier shell correlation for resolution estimation of cryo-EM maps. J. Struct. Biol. *212*, 107579.

Bodon, G., Chassefeyre, R., Pernet-Gallay, K., Martinelli, N., Effantin, G., Hulsik, D.L., Belly, A., Goldberg, Y., Chatellard-Causse, C., Blot, B., et al. (2011). Charged multivesicular body protein 2B (CHMP2B) of the endosomal sorting complex required for transport-III (ESCRT-III) polymerizes into helical structures deforming the plasma membrane. J. Biol. Chem. *286*, 40276–40286.

Brissette, J.L., Russel, M., Weiner, L., and Model, P. (1990). Phage shock protein, a stress protein of Escherichia coli. Proc. Natl. Acad. Sci. USA *87*, 862–866.

Brissette, J.L., Weiner, L., Ripmaster, T.L., and Model, P. (1991). Characterization and sequence of the Escherichia coli stress-induced psp operon. J. Mol. Biol. *220*, 35–48.

Bultema, J.B., Fuhrmann, E., Boekema, E.J., and Schneider, D. (2010). Vipp1 and PspA: Related but not twins. Commun. Integr. Biol. *3*, 162–165.

Caillat, C., Maity, S., Miguet, N., Roos, W.H., and Weissenhorn, W. (2019). The role of VPS4 in ESCRT-III polymer remodeling. Biochem. Soc. Trans. *47*, 441–448.

Carlton, J.G., and Martin-Serrano, J. (2007). Parallels between cytokinesis and retroviral budding: a role for the ESCRT machinery. Science *316*, 1908–1912.

Darwin, A.J. (2005). The phage-shock-protein response. Mol. Microbiol. *57*, 621–628.

Desfosses, A., Ciuffa, R., Gutsche, I., and Sachse, C. (2014). SPRING – An image processing package for single-particle based helical reconstruction from electron cryomicrographs. J. Struct. Biol. *185*, 15–26.

Di Tommaso, P., Moretti, S., Xenarios, I., Orobitg, M., Montanyola, A., Chang, J.-M., Taly, J.-F., and Notredame, C. (2011). T-Coffee: a web server for the multiple sequence alignment of protein and RNA sequences using structural information and homology extension. Nucleic Acids Res. *39*, W13-7.

Elderkin, S., Jones, S., Schumacher, J., Studholme, D., and Buck, M. (2002). Mechanism of action of the Escherichia coli phage shock protein PspA in repression of the AAA family transcription factor PspF. J. Mol. Biol. *320*, 23–37.

Engl, C., Jovanovic, G., Lloyd, L.J., Murray, H., Spitaler, M., Ying, L., Errington, J., and Buck, M. (2009). In vivo localizations of membrane stress controllers PspA and PspG in Escherichia coli. Mol. Microbiol. *73*, 382–396.

Emsley, P., Lohkamp, B., Scott, W.G., and Cowtan, K. (2010). Features and development of *Coot*. Acta Crystallogr. D Biol. Crystallogr. *66*, 486–501.

Engl, C., Beek, A.T., Bekker, M., de Mattos, J.T., Jovanovic, G., and Buck, M. (2011). Dissipation of proton motive force is not sufficient to induce the phage shock protein response in Escherichia coli. Curr. Microbiol. *62*, 1374–1385.

Ford, M.G.J., Mills, I.G., Peter, B.J., Vallis, Y., Praefcke, G.J.K., Evans, P.R., and McMahon, H.T. (2002). Curvature of clathrin-coated pits driven by epsin. Nature *419*, 361–366.

Frost, A., Unger, V.M., and De Camilli, P. (2009). The BAR domain superfamily: membrane-molding macromolecules. Cell *137*, 191–196.

Fuhrmann, E., Bultema, J.B., Kahmann, U., Rupprecht, E., Boekema, E.J., and Schneider, D. (2009). The vesicle-inducing protein 1 from Synechocystis sp. PCC 6803 organizes into diverse higher-ordered ring structures. Mol. Biol. Cell *20*, 4620–4628.

Garrus, J.E., von Schwedler, U.K., Pornillos, O.W., Morham, S.G., Zavitz, K.H., Wang, H.E., Wettstein, D.A., Stray, K.M., Côté, M., Rich, R.L., et al. (2001). Tsg101 and the vacuolar protein sorting pathway are essential for HIV-1 budding. Cell *107*, 55–65.

Gautier, R., Douguet, D., Antonny, B., and Drin, G. (2008). HELIQUEST: a web server to screen sequences with specific alpha-helical properties. Bioinformatics *24*, 2101–2102.

Ghazi-Tabatabai, S., Saksena, S., Short, J.M., Pobbati, A.V., Veprintsev, D.B., Crowther, R.A., Emr, S.D., Egelman, E.H., and Williams, R.L. (2008). Structure and disassembly of filaments formed by the ESCRT-III subunit Vps24. Structure *16*, 1345–1356.

Goddard, T.D., Huang, C.C., Meng, E.C., Pettersen, E.F., Couch, G.S., Morris, J.H., and Ferrin, T.E. (2018). UCSF ChimeraX: Meeting modern challenges in visualization and analysis. Protein Sci. *27*, 14–25.

Guo, L., and Bramkamp, M. (2019). Bacterial dynamin-like protein DynA mediates lipid and content mixing. FASEB J. *33*, 11746–11757.

Gupta, T.K., Klumpe, S., Gries, K., Heinz, S., Wietrzynski, W., Ohnishi, N., Niemeyer, J., Spaniol, B., Schaffer, M., Rast, A., et al. (2021). Structural basis for VIPP1 oligomerization and maintenance of thylakoid membrane integrity. Cell. https://doi.org/10.1016/j.cell.2021.05.011.

Gutu, A., Chang, F., and O'Shea, E.K. (2018). Dynamical localization of a thylakoid membrane binding protein is required for acquisition of photosynthetic competency. Mol. Microbiol. *108*, 16–31.

Hagen, W.J.H., Wan, W., and Briggs, J.A.G. (2017). Implementation of a cryo-electron tomography tilt-scheme optimized for high resolution subtomogram averaging. J. Struct. Biol. *197*, 191–198.

Hankamer, B.D., Elderkin, S.L., Buck, M., and Nield, J. (2004). Organization of the AAA(+) adaptor protein PspA is an oligomeric ring. J. Biol. Chem. *279*, 8862–8866.

Heidrich, J., Thurotte, A., and Schneider, D. (2017). Specific interaction of IM30/Vipp1 with cyanobacterial and chloroplast membranes results in membrane remodeling and eventually in membrane fusion. Biochim. Biophys. Acta Biomembr. *1859*, 537–549.

Heidrich, J., Wulf, V., Hennig, R., Saur, M., Markl, J., Sönnichsen, C., and Schneider, D. (2016). Organization into higher ordered ring structures counteracts membrane binding of IM30, a protein associated with inner membranes in chloroplasts and cyanobacteria. J. Biol. Chem. *291*, 14954–14962.

Henne, W.M., Buchkovich, N.J., and Emr, S.D. (2011). The ESCRT pathway. Dev. Cell *21*, 77–91.

Hennig, R., Heidrich, J., Saur, M., Schmüser, L., Roeters, S.J., Hellmann, N., Woutersen, S., Bonn, M., Weidner, T., Markl, J., and Schneider, D. (2015). IM30 triggers membrane fusion in cyanobacteria and chloroplasts. Nat. Commun. *6*, 7018.

Huber, S.T., Mostafavi, S., Mortensen, S.A., and Sachse, C. (2020). Structure and assembly of ESCRT-III helical Vps24 filaments. Sci. Adv. *6*, eaba4897.

Joly, N., Engl, C., Jovanovic, G., Huvet, M., Toni, T., Sheng, X., Stumpf, M.P.H., and Buck, M. (2010). Managing membrane stress: the phage shock protein (Psp) response, from molecular mechanisms to physiology. FEMS Microbiol. Rev. *34*, 797–827.

Jovanovic, G., Mehta, P., McDonald, C., Davidson, A.C., Uzdavinys, P., Ying, L., and Buck, M. (2014). The N-terminal amphipathic helices determine regulatory and effector functions of phage shock protein A (PspA) in Escherichia coli. J. Mol. Biol. *426*, 1498–1511.

Junglas, B., and Schneider, D. (2018). What is Vipp1 good for? Mol. Microbiol. *108*, 1–5.

Junglas, B., Orru, R., Axt, A., Siebenaller, C., Steinchen, W., Heidrich, J., Hellmich, U.A., Hellmann, N., Wolf, E., Weber, S.A.L., and Schneider, D. (2020). IM30 IDPs form a membrane-protective carpet upon super-complex disassembly. Commun. Biol. *3*, 595.

Katzmann, D.J., Babst, M., and Emr, S.D. (2001). Ubiquitin-dependent sorting into the multivesicular body pathway requires the function of a conserved endosomal protein sorting complex, ESCRT-I. Cell *106*, 145–155.

Kleerebezem, M., Crielaard, W., and Tommassen, J. (1996). Involvement of stress protein PspA (phage shock protein A) of Escherichia coli in maintenance of the protonmotive force under stress conditions. EMBO J. *15*, 162–171.

Kobayashi, H., Yamamoto, M., and Aono, R. (1998). Appearance of a stress-response protein, phage-shock protein A, in Escherichia coli exposed to hydrophobic organic solvents. Microbiology (Reading) *144*, 353–359.

Kobayashi, R., Suzuki, T., and Yoshida, M. (2007). Escherichia coli phage-shock protein A (PspA) binds to membrane phospholipids and repairs proton leakage of the damaged membranes. Mol. Microbiol. *66*, 100–109.

Krause, D. (2019). JUWELS: Modular Tier-0/1 Supercomputer at the Jülich Supercomputing Centre. Journal of Large-Scale Research Facilities JLSRF *5*, 135.

Kremer, J.R., Mastronarde, D.N., and McIntosh, J.R. (1996). Computer Visualization of Three-Dimensional Image Data Using IMOD. J. Struct. Biol. *116*, 71–76.

Larkin, M.A., Blackshields, G., Brown, N.P., Chenna, R., McGettigan, P.A., McWilliam, H., Valentin, F., Wallace, I.M., Wilm, A., Lopez, R., et al. (2007). Clustal W and Clustal X version 2.0. Bioinformatics *23*, 2947–2948.

Lata, S., Schoehn, G., Jain, A., Pires, R., Piehler, J., Gottlinger, H.G., and Weissenhorn, W. (2008). Helical structures of ESCRT-III are disassembled by VPS4. Science *321*, 1354–1357.

Liebschner, D., Afonine, P.V., Baker, M.L., Bunkóczi, G., Chen, V.B., Croll, T.I., Hintze, B., Hung, L.W., Jain, S., McCoy, A.J., et al. (2019). Macromolecular structure determination using X-rays, neutrons and electrons: recent developments in Phenix. Acta Crystallogr. D Struct. Biol. *75*, 861–877.

Liu, J., Tassinari, M., Souza, D.P., Naskar, S., Noel, J.K., Bohuszewicz, O., Buck, M., Williams, T.A., Baum, B., and Low, H.H. (2021). Bacterial Vipp1 and PspA are members of the ancient ESCRT-III membrane-remodeling superfamily. Cell. https://doi.org/10.1016/j.cell.2021.05.041.

Lloyd, L.J., Jones, S.E., Jovanovic, G., Gyaneshwar, P., Rolfe, M.D., Thompson, A., Hinton, J.C., and Buck, M. (2004). Identification of a new member of the phage shock protein response in Escherichia coli, the phage shock protein G (PspG). J. Biol. Chem. *279*, 55707–55714.

Ludtke, S.J. (2016). Single-Particle Refinement and Variability Analysis in EMAN2.1. Meth. Enzymol. *579*, 159–189.

Male, A.L., Oyston, P.C.F., and Tavassoli, A. (2014). Self-Assembly of Escherichia coli Phage Shock Protein A. Adv. Microbiol. *04*, 353–359.

Manganelli, R., and Gennaro, M.L. (2017). Protecting from Envelope Stress: Variations on the Phage-Shock-Protein Theme. Trends Microbiol. *25*, 205–216.

Martinez-Sanchez, A., Garcia, I., Asano, S., Lucic, V., and Fernandez, J.-J. (2014). Robust membrane detection based on tensor voting for electron tomography. J. Struct. Biol. *186*, 49–61.

Mastronarde, D.N. (2005). Automated electron microscope tomography using robust prediction of specimen movements. J. Struct. Biol. *152*, 36–51.

McCullough, J., Clippinger, A.K., Talledge, N., Skowyra, M.L., Saunders, M.G., Naismith, T.V., Colf, L.A., Afonine, P., Arthur, C., Sundquist, W.I., et al. (2015). Structure and membrane remodeling activity of ESCRT-III helical polymers. Science *350*, 1548–1551.

McDonald, C., Jovanovic, G., Ces, O., and Buck, M. (2015). Membrane stored curvature elastic stress modulates recruitment of maintenance proteins pspa and vipp1. MBio *6*, e01188-15.

McDonald, C., Jovanovic, G., Wallace, B.A., Ces, O., and Buck, M. (2017). Structure and function of PspA and Vipp1 N-terminal peptides: Insights into the membrane stress sensing and mitigation. Biochim. Biophys. Acta Biomembr. *1859*, 28–39.

Morin, A., Eisenbraun, B., Key, J., Sanschagrin, P.C., Timony, M.A., Ottaviano, M., and Sliz, P. (2013). Collaboration gets the most out of software. eLife *2*, e01456.

Muzioł, T., Pineda-Molina, E., Ravelli, R.B., Zamborlini, A., Usami, Y., Göttlinger, H., and Weissenhorn, W. (2006). Structural basis for budding by the ESCRT-III factor CHMP3. Dev. Cell *10*, 821–830.

Nagai, T., Ibata, K., Park, E.S., Kubota, M., Mikoshiba, K., and Miyawaki, A. (2002). A variant of yellow fluorescent protein with fast and efficient maturation for cell-biological applications. Nat. Biotechnol. *20*, 87–90.

Nguyen, H.C., Talledge, N., McCullough, J., Sharma, A., Moss, F.R., 3rd, Iwasa, J.H., Vershinin, M.D., Sundquist, W.I., and Frost, A. (2020). Membrane constriction and thinning by sequential ESCRT-III polymerization. Nat. Struct. Mol. Biol. *27*, 392–399.

Osadnik, H., Schöpfel, M., Heidrich, E., Mehner, D., Lilie, H., Parthier, C., Risselada, H.J., Grubmüller, H., Stubbs, M.T., and Brüser, T. (2015). PspF-binding domain PspA1-144 and the PspA·F complex: New insights into the coiled-coil-dependent regulation of AAA+ proteins. Mol. Microbiol. *98*, 743–759.

Parasassi, T., De Stasio, G., d'Ubaldo, A., and Gratton, E. (1990). Phase fluctuation in phospholipid membranes revealed by Laurdan fluorescence. Biophys. J. *57*, 1179–1186.

Pettersen, E.F., Goddard, T.D., Huang, C.C., Couch, G.S., Greenblatt, D.M., Meng, E.C., and Ferrin, T.E. (2004). UCSF Chimera—A visualization system for exploratory research and analysis. J. Comput. Chem. *25*, 1605–1612.

Pfitzner, A.-K., Mercier, V., Jiang, X., Moser von Filseck, J., Baum, B., Šarić, A., and Roux, A. (2020). An ESCRT-III Polymerization Sequence Drives Membrane Deformation and Fission. Cell *182*, 1140–1155.e18.

Praefcke, G.J.K., and McMahon, H.T. (2004). The dynamin superfamily: universal membrane tubulation and fission molecules? Nat. Rev. Mol. Cell Biol. *5*, 133–147.

Punjani, A., Rubinstein, J.L., Fleet, D.J., and Brubaker, M.A. (2017). cryoSPARC: algorithms for rapid unsupervised cryo-EM structure determination. Nat. Methods *14*, 290–296.

Rohou, A., and Grigorieff, N. (2015). CTFFIND4: Fast and accurate defocus estimation from electron micrographs. J. Struct. Biol. *192*, 216–221.

Rueden, C.T., Schindelin, J., Hiner, M.C., DeZonia, B.E., Walter, A.E., Arena, E.T., and Eliceiri, K.W. (2017). ImageJ2: ImageJ for the next generation of scientific image data. BMC Bioinformatics *18*, 529.

Šali, A., and Blundell, T.L. (1993). Comparative Protein Modelling by Satisfaction of Spatial Restraints. J. Mol. Biol. *234*, 779–815.

Saur, M., Hennig, R., Young, P., Rusitzka, K., Hellmann, N., Heidrich, J., Morgner, N., Markl, J., and Schneider, D. (2017). A Janus-Faced IM30 Ring Involved in Thylakoid Membrane Fusion Is Assembled from IM30 Tetramers. Structure *25*, 1380–1390.e5.

Siebenaller, C., Junglas, B., and Schneider, D. (2019). Functional Implications of Multiple IM30 Oligomeric States. Front. Plant Sci. *10*, 1500.

Siebenaller, C., Junglas, B., Lehmann, A., Hellmann, N., and Schneider, D. (2020). Proton Leakage Is Sensed by IM30 and Activates IM30-Triggered Membrane Fusion. Int. J. Mol. Sci. *21*, 4530.

Takahashi, Y., He, H., Tang, Z., Hattori, T., Liu, Y., Young, M.M., Serfass, J.M., Chen, L., Gebru, M., Chen, C., et al. (2018). An autophagy assay reveals the ESCRT-III component CHMP2A as a regulator of phagophore closure. Nat. Commun. *9*, 2855.

Tegunov, D., and Cramer, P. (2019). Real-time cryo-electron microscopy data preprocessing with Warp. Nat. Methods *16*, 1146–1152.

Terwilliger, T.C., Ludtke, S.J., Read, R.J., Adams, P.D., and Afonine, P.V. (2020). Improvement of cryo-EM maps by density modification. Nat. Methods *17*, 923–927.

Theis, J., Gupta, T.K., Klingler, J., Wan, W., Albert, S., Keller, S., Engel, B.D., and Schroda, M. (2019). VIPP1 rods engulf membranes containing phosphatidylinositol phosphates. Sci. Rep. *9*, 8725.

Theis, J., Niemeyer, J., Schmollinger, S., Ries, F., Rütgers, M., Gupta, T.K., Sommer, F., Muranaka, L.S., Venn, B., Schulz-Raffelt, M., et al. (2020). VIPP2 interacts with VIPP1 and HSP22E/F at chloroplast membranes and modulates a retrograde signal for *HSP22E/F* gene expression. Plant Cell Environ. *43*, 1212–1229.

Thurotte, A., and Schneider, D. (2019). The fusion activity of IM30 rings involves controlled unmasking of the fusogenic core. Front. Plant Sci. *10*, 108.

Thurotte, A., Brüser, T., Mascher, T., and Schneider, D. (2017). Membrane chaperoning by members of the PspA/IM30 protein family. Commun. Integr. Biol. *10*, e1264546.

Vietri, M., Schink, K.O., Campsteijn, C., Wegner, C.S., Schultz, S.W., Christ, L., Thoresen, S.B., Brech, A., Raiborg, C., and Stenmark, H. (2015). Spastin and ESCRT-III coordinate mitotic spindle disassembly and nuclear envelope sealing. Nature *522*, 231–235.

Vothknecht, U.C., Otters, S., Hennig, R., and Schneider, D. (2012). Vipp1: a very important protein in plastids?!. J. Exp. Bot. *63*, 1699–1712.

Wagner, T., Lusnig, L., Pospich, S., Stabrin, M., Schönfeld, F., and Raunser, S. (2020). Two particle-picking procedures for filamentous proteins: SPHIRE-crYOLO filament mode and SPHIRE-STRIPER. Acta Crystallogr. D Struct. Biol. *76*, 613–620.

Wagner, T., Merino, F., Stabrin, M., Moriya, T., Antoni, C., Apelbaum, A., Hagel, P., Sitsel, O., Raisch, T., Prumbaum, D., et al. (2019). SPHIRE-crYOLO is a fast and accurate fully automated particle picker for cryo-EM. Commun. Biol. *2*, 218.

Waterhouse, A.M., Procter, J.B., Martin, D.M.A., Clamp, M., and Barton, G.J. (2009). Jalview Version 2–a multiple sequence alignment editor and analysis workbench. Bioinformatics *25*, 1189–1191.

Weiner, L., Brissette, J.L., and Model, P. (1991). Stress-induced expression of the Escherichia coli phage shock protein operon is dependent on σ 54 and modulated by positive and negative feedback mechanisms. Genes Dev. *5*, 1912–1923.

Wolf, D., Kalamorz, F., Wecke, T., Juszczak, A., Mäder, U., Homuth, G., Jordan, S., Kirstein, J., Hoppert, M., Voigt, B., et al. (2010). In-depth profiling of the LiaR response of Bacillus subtilis. J. Bacteriol. *192*, 4680–4693.

Yamaguchi, S., Reid, D.A., Rothenberg, E., and Darwin, A.J. (2013). Changes in Psp protein binding partners, localization and behaviour upon activation of the Yersinia enterocolitica phage shock protein response. Mol. Microbiol. *87*, 656–671.

Zhen, Y., Spangenberg, H., Munson, M.J., Brech, A., Schink, K.O., Tan, K.-W., Sørensen, V., Wenzel, E.M., Radulovic, M., Engedal, N., et al. (2020). ESCRT-mediated phagophore sealing during mitophagy. Autophagy *16*, 826–841.

Zhu, W., Krishna, S., Garcia, C., Lin, C.J., Mitchell, B.D., Scott, K.L., Mohila, C.A., Creighton, C.J., Yoo, S.-H., Lee, H.K., and Deneen, B. (2017). Daam2 driven degradation of VHL promotes gliomagenesis. eLife *6*, e31926.

Zivanov, J., Nakane, T., Forsberg, B.O., Kimanius, D., Hagen, W.J.H., Lindahl, E., and Scheres, S.H.W. (2018). New tools for automated high-resolution cryo-EM structure determination in RELION-3. eLife *7*, e42166.

STAR★METHODS

KEY RESOURCES TABLE

REAGENT or RESOURCE	SOURCE	IDENTIFIER
Bacterial and virus strains		
E. coli BL21 (DE3)	NEB	Cat# C2527H
E. coli ΔpspA K-12 JW1297-1	Baba et al., 2006	CGSC# 9162
Chemicals, peptides, and recombinant proteins		
E. coli polar lipid extract (EPL)	Avanti Polar Lipids	Cat# 100600C
DOPC	Avanti Polar Lipids	Cat# 850375C
DOPG	Avanti Polar Lipids	Cat# 840475C
Laurdan	Sigma-Aldrich	Cat# 40227
Synechocystis PspA	This paper	UniProtKB: P74717; Syn:slr1188
Synechocystis PspA_A75S/A78S	This paper	N/A
Deposited data		
Synechocystis PspA structure	This paper	PDB: 7ABK
Synechocystis PspA Filament (apo) map	This paper	EMD: 11698
Synechocystis PspA Filament + Lipid map	This paper	EMD: 12733
E. coli PspA (1-144)	Osadnik et al., 2015	PDB: 4WHE
Human IST1 NTD R16E K27E double mutant	Nguyen et al., 2020	PDB: 6TZA
Human CHMP1B	Nguyen et al., 2020	PDB: 6TZ9
S. cerevisiae Vps24	Huber et al., 2020	PDB: 6ZH3
Recombinant DNA		
pRSET_SynPspA	This paper	N/A
pRSET_SynPspA_A75S/A78S	This paper	N/A
pET50b_SynPspA	This paper	N/A
pBAD_SynPspA-YFP	This paper	N/A
Software and algorithms		
ImageJ	Rueden et al., 2017	https://imagej.nih.gov/ij/
Clustal	Larkin et al., 2007	http://www.clustal.org/
Jalview	Waterhouse et al., 2009	https://www.jalview.org/
HELIQUEST	Gautier et al., 2008	https://heliquest.ipmc.cnrs.fr/
ConSurf	Ashkenazy et al., 2016	https://consurf.tau.ac.il/
OriginPro 2020b	OriginLab Corp.	https://www.originlab.com/2020
RELION 3.0	Zivanov et al., 2018	https://github.com/3dem/relion
cryoSPARC v2.1	Punjani et al., 2017	https://cryosparc.com/
SPRING	Desfosses et al., 2014	https://spring.fz-juelich.de/
E2HELIXBOXER	Ludtke, 2016	https://github.com/cryoem/eman2/blob/master/programs/e2helixboxer.py
crYOLO 1.5	Wagner et al., 2019, 2020	https://cryolo.readthedocs.io/en/stable/
CTFFIND 4.1	Rohou and Grigorieff, 2015	https://grigoriefflab.umassmed.edu/ctffind4
Coot 0.9	Emsley et al., 2010	https://www2.mrc-lmb.cam.ac.uk/personal/pemsley/coot/
MODELER	Šali and Blundell, 1993	https://salilab.org/modeller/
SPOC	Beckers and Sachse, 2020	https://github.com/MaximilianBeckers/SPOC
Phenix 1.16-3549	Afonine et al., 2018a, 2018b; Liebschner et al., 2019; Terwilliger et al., 2020	https://phenix-online.org/
WARP	Tegunov and Cramer, 2019	http://www.warpem.com/warp/

(*Continued on next page*)

Continued		
REAGENT or RESOURCE	SOURCE	IDENTIFIER
TomoSegMemTV	Martinez-Sanchez et al., 2014	https://sites.google.com/site/3demimageprocessing/tomosegmemtv
SerialEM	Mastronarde, 2005	https://bio3d.colorado.edu/SerialEM/
Amira 2020.2	ThermoFisher Scientific	https://www.thermofisher.com/us/en/home/industrial/electron-microscopy/electron-microscopy-instruments-workflow-solutions/3d-visualization-analysis-software/3d-visualization-analysis-software-resource-center/whats-new-amira-avizo-software-20202.html
EPU 2.8.1.10	ThermoFisher Scientific	https://www.thermofisher.com/de/de/home/electron-microscopy/products/software-em-3d-vis/epu-software.html
UCSF ChimeraX	Goddard et al., 2018	https://rbvi.ucsf.edu/chimerax/
UCSF Chimera	Pettersen et al., 2004	https://www.cgl.ucsf.edu/chimera/
Other		
Quantifoil Grids R1.2/1.3 Cu 200 mesh	Electron Microscopy Sciences	Cat# Q2100CR1.3S
Quantifoil Grids R2/2 Cu 300 mesh	Electron Microscopy Sciences	Cat# Q3100CR2S
Lacey Carbon Grids Cu 200 mesh	Electron Microscopy Sciences	Cat# LC200-Cu
Continuous Carbon Grids Cu 300 mesh	Electron Microscopy Sciences	Cat# CF300-Cu

RESOURCE AVAILABILITY

Lead contact

Further information and requests for resources and reagents should be directed to and will be fulfilled by the Lead Contact, Carsten Sachse (c.sachse@fz-juelich.de).

Materials availability

All unique and stable reagents generated in this study are available from the Lead Contact with a completed Material Transfer Agreement.

Data and code availability

The EMDB accession numbers for the 3.6 Å resolution cryo-EM map and PspA model are EMD: 11698 and PDB: 7ABK. The 7.2 Å map of PspA in the presence of *E. coli* polar lipids has the EMD:12733 ID.

EXPERIMENTAL MODEL AND SUBJECT DETAILS

Bacterial cells

E. coli BL21 (DE3) cells and *E. coli ΔpspA* K-12 JW1297 strain (Baba et al., 2006) via an inducible L-arabinose promotor were used in this study. For recombinant protein expression, *E. coli BL21 (DE3)* cells carrying the respective expression plasmid (pRSET_SynPspA, pRSET_SynPspA_A75S/A78S or pET50b_SynPspA) were grown to an OD_{600} of 0.6 - 0.8 at 37°C in TB or LB medium plus antibiotics. Protein expression was induced by adding 0.5 or 1 mM IPTG and overnight incubation at 30°C. *E. coli ΔpspA* K-12 JW1297 strain and *E. coli ΔpspA* K-12 JW1297 cells carrying the pBAD_SynPspA-YFP plasmid were grown overnight in LB medium at 37°C. The preculture was diluted 1:100 in fresh LB to an OD_{600} of 0.45. SynPspA-YFP expression was induced by addition of 0.02% L-arabinose. 30 min after induction, samples were taken for fluorescence microscopy imaging.

METHOD DETAILS

Expression and purification of PspA

PspA wt (*slr1188*) of *Synechocystis* sp. PCC 6803 and PspA_A75S/A78S were heterologously expressed in *E. coli* BL21 (DE3) cells in LB or TB medium using a pRSET6 plasmid.

For native extraction of PspA rods, cells were resuspended in lysis buffer I (50 mM sodium phosphate, 300 mM NaCl, pH 7.6) supplemented with a protease inhibitor cocktail (Sigma) and lysed in a cell disruptor (TS Constant Cell disruption systems 1.1 KW; Constant Systems). The lysate was cleared by centrifugation for 15 min at 5000 g. The cleared lysate was incubated overnight

at 4°C. Rods were pelleted by centrifugation for 15 min at 5000 g. The pellet was resuspended in 50 mM sodium phosphate, 1000 mM NaCl at pH 7.6. The resulting suspension was concentrated by ultracentrifugation (Vivaspin centrifugal filter units MWCO 10 kDa) and washed thoroughly with 10 mM sodium phosphate pH 7.6. The crude rod extract was further purified by differential centrifugation: large particles and aggregates were sedimented by centrifugation for 20 min at 20,000 g; shorter rods by centrifugation for 60 min at 49,000 g. As a final polishing step, the rods were diluted and incubated with 0.5% Triton X-100 overnight. Again, large particles and aggregates were removed by low-speed centrifugation for 60 min at 20,000 g; rods were pelleted and washed twice with 10 mM sodium phosphate pH 7.6.

For purification of PspA and PspA_A75S/A78S under denaturing conditions, cells were resuspended in lysis buffer containing 6 M urea (50 mM sodium phosphate, 300 mM NaCl, 6 M urea, 1% CHAPS (w/w), 75 mM NaSCN, pH 7.6) supplemented with a protease inhibitor. Cells were lysed in a cell disruptor (TS Constant Cell disruption systems 1.1 KW; Constant Systems) or by tip-sonication (Branson sonifier). The lysate was cleared by centrifugation for 15 min at 5000 g. The supernatant was incubated with Ni-NTA agarose beads on an overhead shaker for 1 - 2 h at 4°C. The Ni-NTA matrix was washed with lysis buffer II, wash buffer I (50 mM sodium phosphate, 300 mM NaCl, 6 M urea, 1% CHAPS (w/w), 75 mM NaSCN, 20 mM imidazole, pH 7.6) and wash buffer II (50 mM sodium phosphate, 300 mM NaCl, 75 mM NaSCN, 6 M urea, 60 mM imidazole, pH 7.6). The protein was eluted from the Ni-NTA beads with elution buffer I (50 mM sodium phosphate, 300 mM NaCl, 75 mM NaSCN, 4 M urea, 500 mM imidazole, pH 7.6). The fractions containing protein were pooled and dialyzed overnight against 10 mM sodium phosphate pH 7.6 (100 kDa MWCO). When necessary, protein was concentrated by centrifugation at 20,000 g for 1 h followed by carefully resuspending the pellet in the desired volume of sodium phosphate buffer.

For the cleavage-induced assembly experiments, PspA was expressed in *E. coli* BL21 (DE3) cells in TB medium using a pET50b plasmid. The pET50b plasmid contains an N-terminal NusA-tag connected to the insert via a 6x His-tag and a 3C cleavage site. For purification of the NusA-PspA fusion protein, cells were resuspended in lysis buffer I supplemented with a protease inhibitor. Cells were lysed in a cell disruptor (TS Constant Cell disruption systems 1.1 KW; Constant Systems). The lysate was cleared by centrifugation for 15 min at 5000 g. The supernatant was incubated with Ni-NTA agarose beads on an overhead shaker for 30 min at 4°C. The Ni-NTA matrix was washed with lysis buffer, wash buffer III (50 mM sodium phosphate, 300 mM NaCl, 20 mM imidazole, pH 7.6) and wash buffer IV (50 mM sodium phosphate, 300 mM NaCl, 60 mM imidazole, pH 7.6). The protein was eluted from the Ni-NTA beads with elution buffer II (50 mM sodium phosphate, 300 mM NaCl, 1000 mM Imidazole, pH 7.6). The fractions containing protein were pooled and dialyzed overnight against 10 mM sodium phosphate pH 7.6 (100 kDa MWCO). When necessary, protein was concentrated by ultracentrifugation (Vivaspin centrifugal filter units MWCO 30 kDa). After the purification procedure, proteins were flash frozen in liquid nitrogen and stored until use at −20°C.

Lipid reconstitution

Chloroform dissolved *E. coli* polar lipid (EPL) extract, DOPC (1,2-dioleoyl-sn-glycero-3-phosphocholine), and DOPG (1,2-dioleoyl-sn-glycero-3-phospho-(1'-rac-glycerol)) were purchased from Avanti polar lipids. Lipid films were produced by evaporating the solvent under a gentle stream of nitrogen and vacuum desiccation overnight. The lipid films were rehydrated in 10 mM sodium phosphate pH 7.6 by shaking for 30 mins at 37°C. The resulting liposome solution was subjected to five freeze-thaw cycles, combined with sonication at 37°C in a bath sonicator. SUVs (small unilamellar vesicles) or LUVs (large unilamellar vesicles) were generated by extrusion of the liposome solution through a porous polycarbonate filter (50 nm or 400 nm pores). For cryo-EM analyses, PspA rods (0.8 mg/mL) were incubated with EPL vesicles (5 mg/mL) for at least 2 h at room temperature.

Membrane binding assay

In order to analyze the membrane binding propensities of PspA, liposomes containing 100% DOPC or a mixture of 40 mol% DOPG and 60 mol% DOPC, each containing additionally 0.2 mol% of the fluorescent dye Laurdan (6-Dodecanoyl-N,N-dimethyl-2-naphthylamine, from Sigma, Taufkirchen, Germany), were prepared from lipid films as described above. The fluorescent properties of Laurdan depend on the membrane structure, and changes in the membrane state, here caused by membrane binding of PspA, can be used to assess the membrane binding of proteins (Heidrich et al., 2016). After the five freeze-thaw cylces, PspA was added to the liposome solution with a final concentration of 100 μM lipid, and protein concentrations as indicated. After incubation at room temperature for 2 h, corrected fluorescence emission spectra were recorded using a Jasco FP8500 fluorescence spectrometer (Jasco, Pfungstadt, Germany), with an excitation wavelength of 350 nm and an increment of 1 nm. GP (generalized polarization) values (Parasassi et al., 1990) were calculated based on the mean intensities recorded in the wavelength interval 438-442 nm and 488-492 nm, yielding I_{440} and I_{490}, respectively, according to $GP = (I_{440}-I_{490})/(I_{440}+I_{490})$. A one-site binding model was used to determine the apparent affinity (K_D) of PspA to lipid membranes.

Cleavage-induced assembly of PspA rods (CIA-PspA)

For the generation of CIA-PspA rods, NusA-PspA was cleaved by 3C protease to produce NusA and free PspA. The reaction was conducted in the presence of EPL vesicles: A mixture of NusA-PspA (1 mg/mL), EPL SUVs (5 mg/mL) and 3C protease (0.5 mg/mL) was incubated at 37°C with shaking for at least 2 h. Samples of the reaction mixture were analyzed by cryo-EM.

Fluorescence microscopy

For fluorescence microscopy, PspA wt and mutant were genetically fused to a yellow fluorescent protein (YFP, Venus) (Nagai et al., 2002) and expressed using a pBAD vector (Invitrogen) (pBAD_SynPspA-YFP). Proteins were expressed at a low level in an *E. coli ΔpspA* K-12 JW1297 strain (Baba et al., 2006) via addition of 0.02% L-arabinose. 5 μL cell suspension with an OD_{600} = 0.6 were added to 2% agarose pads on a microscope glass slide, and PspA-YFP localization was analyzed using an inverted phase contrast fluorescence microscope (Zeiss Axio Observer.Z1). Fluorescence microscopy images shown in Figure S1A are composites of bright field images and YFP-channel images (excitation filter 450 - 490 nm, emission filter 500 - 550 nm, 500 ms exposure time).

Negative staining electron microscopy

For negative staining electron microscopy, 3 μL sample was applied to glow-discharged (PELCO easiGlow Glow Discharger,Ted Pella Inc.) continuous carbon grids (CF-300 Cu, Electron Microscopy Sciences). The sample was incubated on the grid for 1 min. Then the grid was side-blotted using filter paper, washed with 3 μL water and stained with 3 μL 2% uranyl acetate for 30 s and air-dried. The grids were imaged with a 120 kV Talos L120C electron microscope (ThermoFischer Scientific/FEI) equipped with a CETA camera at a pixel size of 4.06 Å/pixel (36,000 x magnification) at an underfocus of 1.0 to 2.5 μm.

Electron cryo-microscopy

Samples for the full high-resolution dataset of PspA rods were prepared by applying 3 μL PspA rods (~7.9 mg/mL) to glow-discharged (PELCO easiGlow Glow Discharger, Ted Pella Inc.) Quantifoil grids (R1.2/1.3 Cu 200 mesh, Electron Microscopy Sciences). The grids were plunge-frozen in liquid ethane using a ThermoFisher Scientific Vitrobot Mark IV set to 90% humidity at 10°C (blotting force −10, blotting time 3 s). A total of 8,342 micrographs were recorded on a 200 kV Talos Arctica G2 (ThermoFisher Scientific) electron microscope equipped with a Bioquantum K3 (Gatan) detector operated by SerialEM (Mastronarde, 2005). Micrographs were collected as 50-frame movies in superresolution mode at 0.419 Å/pixel and a cumulative dose of 50 $e^{-}/Å^2$ and a nominal underfocus of 0.2 to 2.3 μm. Samples of an initial cryo-electron microscopy dataset used for symmetry determination were prepared on Lacey Carbon grids (Electron Microscopy Sciences) and imaged using a Titan Krios (300 kV, FEG) cryo-electron microscope (FEI/Thermo Fischer Scientific), equipped with a Gatan Quantum K2 energy-filtered direct detector. A total of 936 micrographs with a pixel size of 1.35 Å were collected at an underfocus range from 0.8 to 2.6 μm. For cryo-EM of the PspA-liposome mixtures, 3.5 μL sample were applied to glow-discharged (PELCO easiGlow Glow Discharger, Ted Pella Inc.) lacey carbon Cu 200 mesh grids or R2/2 Cu 300 mesh grids (Electron Microscopy Sciences). Excess sample was manually blotted at the back side of the grid for 12 s using filter paper. Plunge-freezing in liquid ethane was performed using a ThermoFisher Scientific Vitrobot Mark IV, set at 100% humidity and 22°C temperature. Frozen grids were stored at liquid nitrogen temperature before usage. Grids were imaged on a 200 kV Talos Arctica G2 (ThermoFisher Scientific) electron microscope equipped with a Bioquantum K3 (Gatan) detector (or with a CETA camera at a pixel size of 2.53 Å/pixel for LUV imaging). For the SUVs (1525 micrographs), SUVs+PspA (1531 micrographs) and SUVs+CIA-PspA (1889 micrographs) datasets micrographs were collected as 50-frame movies in superresolution mode at 0.681 Å/pixel and a cumulative dose of 30 to 32 $e^{-}/Å^2$ and a nominal underfocus of 2.0 to 3.0 μm.

Electron cryo-tomography (cryo-ET)

Before plunge freezing, 5 nm BSA-Gold fiducials (OD 75, 1:50 (v/v)) were added to each incubation mixture directly. Samples were prepared by applying 3.5 μL sample solution to glow-discharged (PELCO easiGlow Glow Discharger, Ted Pella Inc.) lacey carbon Cu 200 mesh grids or R2/2 Cu 300 mesh grids ((Electron Microscopy Sciences). The excess of liquid was removed by manually back-side blotting for 12 s. Grids were immediately vitrified by plunge freezing in liquid ethane at 77 K using a ThermoFisher Scientific Vitrobot Mark IV operated at 100% humidity and 22°C temperature. Frozen grids were stored at liquid nitrogen temperature before usage. Electron microscopy was performed using a Talos Arctica G2 (ThermoFisher Scientific), equipped with a Bioquantum K3 (Gatan), at 200 kV. Tilt series were acquired using a dose symmetric scheme (Hagen et al., 2017), starting at 0° and alternating tilts to ± 60° with an angular increment of 2° at a nominal underfocus of 3.0 μm, in superresolution mode and dose fractionation (up to 6 frames/image), with an object pixel size of 1.362 Å/pixel. The accumulated electron dose for each tilt series did not exceed 120 $e^{-}/Å^2$. SerialEM (Mastronarde, 2005) was used for automated data acquisition.

Image processing and helical reconstruction

The detailed helical reconstruction processing workflow is presented in Figures S1B–S1D. In order to determine the symmetry parameters, a small dataset of 936 micrographs was utilized (Titan Krios/K2) and PspA rods were picked manually in RELION 3.0 (Zivanov et al., 2018) and segmented with a step size of 35 Å into 39,600 windows (Test Dataset A, Figure S1D). The segments were subjected to two rounds of 2D classification. Only classes showing clear secondary structure features and consistent widths were selected. The helical symmetry was determined by analyzing layer lines in the power spectra of the best 2D class and several possible symmetry solutions were obtained using SEGCLASSRECONSTRUCT from the SPRING package (Desfosses et al., 2014). Those symmetry solutions were tested systematically in RELION 3.0 (Zivanov et al., 2018). Using the initial symmetry parameters of 30 Å pitch with 10.25 units per turn, the refinement yielded a map with secondary structure features at 7.3 Å resolution whereas other

solutions did not. This initial model was further refined by two rounds of 3D classifications in RELION 3.0. This procedure resulted in an intermediate map of 6.1 Å resolution (FSC = 0.143) and refined helical symmetry parameters with a 30.1 Å pitch and 10.19 units per turn corresponding to 2.9 Å rise and 35.3° rotation.

Acquired frames of the full 8,342 micrograph dataset (Talos Arctica/K3) (Figure S1D) were preprocessed in WARP by binning to the physical pixel size of 0.839 Å/pixel, frame alignment and correcting for beam-induced motion and stage drift (Tegunov and Cramer, 2019). A subset of the resulting micrographs was subjected to manual filament tracing using E2HELIXBOXER (Ludtke, 2016). Manually traced filaments were used for neural network training and subsequent automated tracing with crYOLO 1.5 (Wagner et al., 2019, 2020). This way, a total of 55,800 rods were detected. After contrast-transfer function (CTF) determination of the micrographs with CTFFIND 4.1 (Rohou and Grigorieff, 2015) and selection of micrographs based on ice quality and image drift (8,257 micrographs), 1.5 million segments (à 450 pixel dimension, at a step size of seven asymmetric units given the 3 Å rise) were extracted from these rods in RELION 3.0 (Zivanov et al., 2018). In a first round of 2D classification, junk particles and classes showing segments with widths > 23 nm and < 19 nm were discarded and only classes showing clear secondary structure features and power spectra were chosen for further processing (Dataset B, 334,000 segments, Figure S1D). A simulated helical cylinder was created from the symmetry parameters (2.9 Å rise and 35.2° rotation obtained from Test Dataset A) and used as a reference for 3D classification. This initial reference was further refined by several rounds of 3D classification and subsequent 3D refinement. Finally, one 3D class resulted in a map showing clear pitch in the α helices at 4.7 Å resolution (19,900 segments). The segments of this class were subjected to multiple rounds of per-particle CTF refinement, Bayesian polishing and 3D auto-refinement focusing on the central 30% of the cylinder using a mask. Fourier shell correlation (FSC) curves were calculated within the mask containing the central 30% of the density and local resolutions were determined using RELION's implementation and rendered in ChimeraX (Goddard et al., 2018). The final map was determined to have a global resolution of 3.6 Å (FSC = 0.143) (helical symmetry: 2.9 Å rise and 35.3° twist).

For helical reconstruction of PspA in presence of EPL SUVs, a dataset of 1531 micrographs was analyzed using cryoSPARC v3.1 (Punjani et al., 2017). Super-resolution movie frames were corrected for beam-induced motion and stage drift, aligned and binned to the physical pixel size of 1.362 Å/pixel. After CTF estimation (using patch-CTF estimation), 17 micrographs were used to manually pick rods and subsequently segmented. 2D averages from those segments were used as templates for automated filament tracing. 917,000 segments were extracted (à 350 pixel dimension, at a step size 30 Å). In a first round of 2D classification, junk particles and poorly aligned particles were discarded. The resulting 548,000 segments were subjected to multiple rounds of 2D classifications to sort them in two major rod classes (Figures S5C–S5E). Class A contained 155,000 segments and class B contained 291,000 segments. Initial 3D volumes for both rod classes were generated starting from a cylinder with 220 Å and 275 Å diameter, respectively. The initial 3D volumes were used for helical symmetry searches using cryoSPARC. The symmetry search outcome was used as starting point for helical refinement starting with the best reconstruction/symmetry parameters and subjecting it iteratively to another symmetry search/helical refinement. Class A yielded a minimum at 2.9 Å rise and 35.2° twist and was refined to 7.7 Å global resolution. At this resolution level, class A was indistinguishable from the reconstruction of PspA alone. Class B yielded a minimum at 4.4 Å rise and 26.6° twist. The helical symmetry was validated by comparing the power spectrum of 2D class averages with simulated layer lines of the identified helical symmetry using SPRING (Figure S5E). Class B was refined to 7.15 Å global resolution using dynamic masking with a z-clip fraction of 0.4.

Cryo-EM map interpretation and model building

The handedness of the final reconstruction of PspA alone was validated by rigid-body fitting the X-ray structure of the *Eco*PspA hairpin structure (Osadnik et al., 2015) (PDB: 4WHE) by Chimera (Pettersen et al., 2004). The 3D reconstruction was B-factor sharpened (B = −98 Å^2) in RELION 3.0 (Zivanov et al., 2018), autosharpened in *phenix.auto_sharpen* (Liebschner et al., 2019; Terwilliger et al., 2020) in Phenix 1.16-3549 and FDR-FSC filtered using SPOC (Beckers and Sachse, 2020). The resulting three maps were used for *de novo* model building in Coot 0.9 (Emsley et al., 2010) for residues 22 - 217. Refinement was performed in *phenix.real_space_refine* (Afonine et al., 2018a) against the *phenix.auto_sharpen* map after symmetry neighbors were created with *phenix.apply_ncs* (Helical 35.3°; 2.9 Å) using default parameters. After two cycles of refinement and manual inspection, the final model was validated in *phenix.validation_cryoem* (Afonine et al., 2018b) (Table S1).

The handedness of the reconstruction of PspA+EPL (class B) was validated by rigid-body fitting the structure of PspA alone by Chimera. To adjust the structure of PspA alone to the new reconstruction α1+2, α3, α4 and α5 were treated as separate bodies and fitted to the density map and the loop regions were recreated using MODELER (Šali and Blundell, 1993). PspA+EPL (class B) was built as a two-start helix, with one strand showing density extending from helix α1 to the inner volume of the rod. An ideal α-helix was built representing helix α0 using Chimera and fitted to this density, followed by building the loop between α0 and α1 with MODELER. By this approach, we obtained a nearly full-length model of PspA including residues 1-217.

The Coulomb potential of a PspA 10-mer (PspA alone) and a PspA 14-mer (PspA+EPL class B) was calculated in Chimera using the built-in ''Coulombic Surface Coloring'' routine with standard settings. The resulting electrostatic potential grid was sampled on the surface of PspA maps in ChimeraX. Structure rendering was done in ChimeraX or Chimera (Goddard et al., 2018; Pettersen et al., 2004). Image processing, helical reconstruction and model building was completed using SBGrid-supported applications (Morin et al., 2013).

Cryo-ET image processing

Frame alignment and averaging was done in WARP (Tegunov and Cramer, 2019). A total of 101 tilt series were analyzed (SUVs: 8, SUVs+PspA: 41, SUVs+CIA-PspA: 52). Tilt series were aligned using gold fiducial markers and down-sampled tomograms were reconstructed ((10.8 Å)^3/voxel) by back projection using the IMOD package (Kremer et al., 1996). Membranes and associated densities were semi-automatically segmented using a tensor voting algorithm *TomoSegMemTV* (Martinez-Sanchez et al., 2014). Output labels were further segmented by visual inspection in combination with denoised tomograms (anisotropic diffusion filtering; diffusion stop threshold 0.3; number of iterations 3) using Amira 2020.2 (FEI SAS/ThermoFisher Scientific). Density profiles of PspA rods were measured using ImageJ (Rueden et al., 2017). They were taken perpendicularly to the rod axis at the central position after averaging 5 slices in z direction and over 100 pixel of rod length.

Image analysis of membranes

To quantitatively assess the size and size changes of EPL vesicles upon addition of PspA, minimum and maximum widths of liposomes, as well as their perimeter, were measured using ImageJ (Rueden et al., 2017). Statistical analyses of the vesicle perimeters were done by testing the null hypothesis (two sample t test) for each pair of the subsets (EPL, EPL+PspA, EPL+PspA (d > 5 nm)) as implemented in OriginPro 2020b. To determine the bilayer leaflet distance, micrographs of the vesicle containing samples ((EPL (1525 micrographs), EPL+PspA (1531 micrographs) and EPL+CIA-PspA (1889 micrographs)) were analyzed using cryoSPARC v3.1 (Punjani et al., 2017). Super-resolution movie frames were corrected for beam-induced motion and stage drift, aligned and binned to the physical pixel size of 1.362 Å/pixel. After CTF estimation (using patch-CTF estimation), 12-36 micrographs were used to manually pick bilayers and subsequently segmented. 2D averages from those segments were used as templates for automated filament tracing. 139,000 (EPL), 832,000 (EPL+PspA) and 4.6 million (EPL+CIA-PspA) segments were extracted (à 200 pixel dimension, at a step size 10 Å). Multiple rounds of 2D classifications were used to remove junk particles and poorly aligned particles. The final subsets contained 99,000 (EPL), 451,000 (EPL+PspA) and 3.8 million (EPL+CIA-PspA) segments in 7-22 classes (Figure S3C).

For analysis of LUVs, the bilayer was traced manually in RELION 3.0 using the filament-picking option (Zivanov et al., 2018). From these traces, segments were extracted every 20 Å with a box size of 100 px at 2.53 Å/pixel yielding 9,963 segments of vesicles only, 8,571 segments of small vesicles and PspA and 17,056 segments of large vesicles and PspA. Bilayer segments were CTF corrected based on micrograph CTF determination (CTFFIND 4.1) (Rohou and Grigorieff, 2015) and subsequently subjected to 2D classification in RELION 3.0 (Zivanov et al., 2018) (Figures S4B and S4C).

Relative density profiles of the class averages were analyzed in OriginPro 2020b using the ''Multiple Peak Fit'' tool with a Gauss peak function. The leaflet distance *d* was measured as the distance between two peak centers in each class average. Leaflet distances of the classes were binned in 0.5 nm groups and plotted versus their relative frequency in each group (Figures S3C, S3D, and S4B).

QUANTIFICATION AND STATISTICAL ANALYSIS

Data and statistical analysis were performed using OriginPro 2020b (OriginLab Corp., Northampton, USA). Detailed descriptions of quantifications and statistical analyses (exact values of *n*, dispersion and precision measures used and statistical tests used) can be found in the respective Figures, Figure legends and Methods section.

Supplemental figures

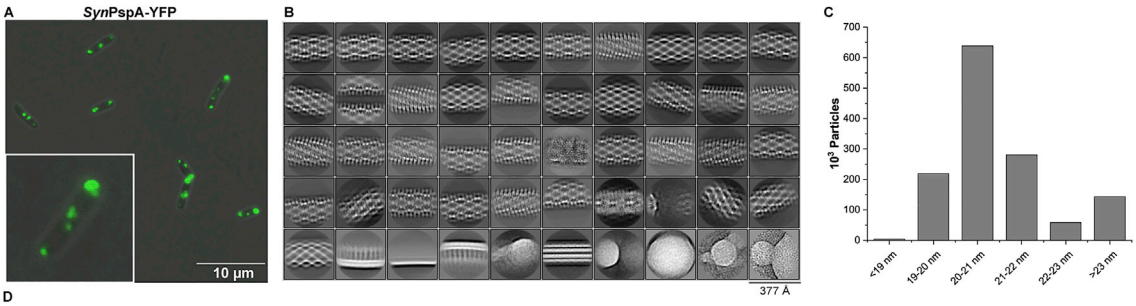

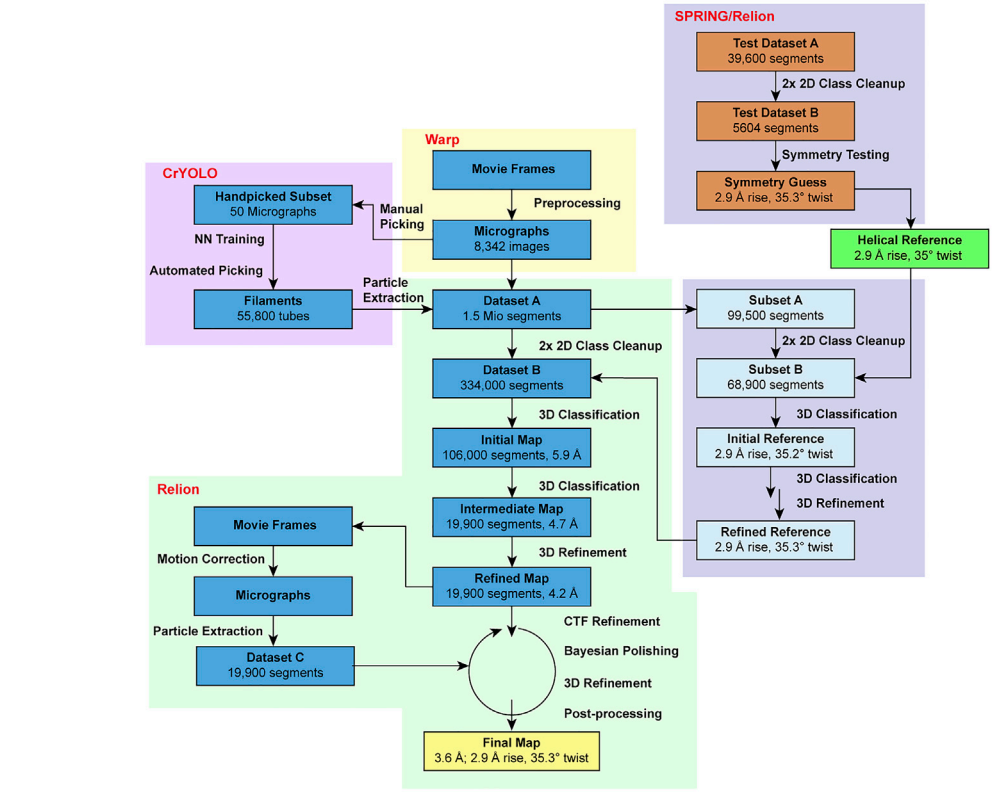

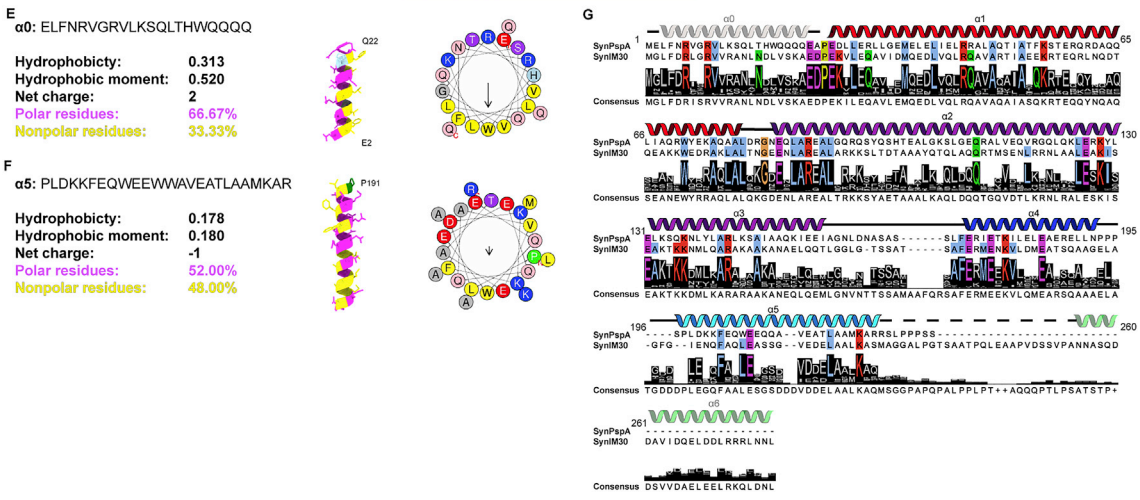

(legend on next page)

Figure S1. Fluorescence microscopy images, processing details, and sequence alignment of PspA, related to Figures 1, 2, and 3

(A) Epifluorescence images of *E. coli* Δ*pspA* cells expressing *Syn*PspA YFP-tagged at the C terminus. Low-level expression of the fusion proteins was induced after addition of 0.02% L-arabinose. Green fluorescent foci are visible within cells, representing higher-ordered PspA assemblies. Typically, *E. coli* cells contain two foci (71%, of n = 197 cells), one localized at each cell pole. In case of dividing cells, fluorescent foci are also visible at the division septum (i.e., the new cell pole) within each daughter cell. (B) Gallery of 2D class averages from initial 1.5 million segment dataset. (C) Histogram showing distribution of measured widths of PspA rods. (D) Basic image processing workflow of PspA structure determination: PspA rods were segmented and a subset subjected to symmetry determination in SPRING followed by symmetry refinement in RELION. Once the symmetry was determined, RELION was used for final 3D structure determination of PspA including CTF refinement and Bayesian polishing. (E) Helix wheel projection of the predicted helix α0. (F) Helix wheel projection of helix α5. Projections were generated with HELIQUEST (Gautier et al., 2008). (G) A conservation query for the PspA/IM30 protein was subjected to the ConSurf server (Ashkenazy et al., 2016) using the *Syn*PspA and the *Syn*IM30 sequence as input. The output of 250 sequences was aligned using ClustalW (Larkin et al., 2007) The resulting consensus sequence together with the *Syn*PspA and *Syn*IM30 were visualized in Jalview (Waterhouse et al., 2009) and superimposed with the PspA/IM30 secondary structure using the ESCRT-III helix nomenclature. Residues with > 90% identity are colored by their properties according to the ClustalX color scheme.

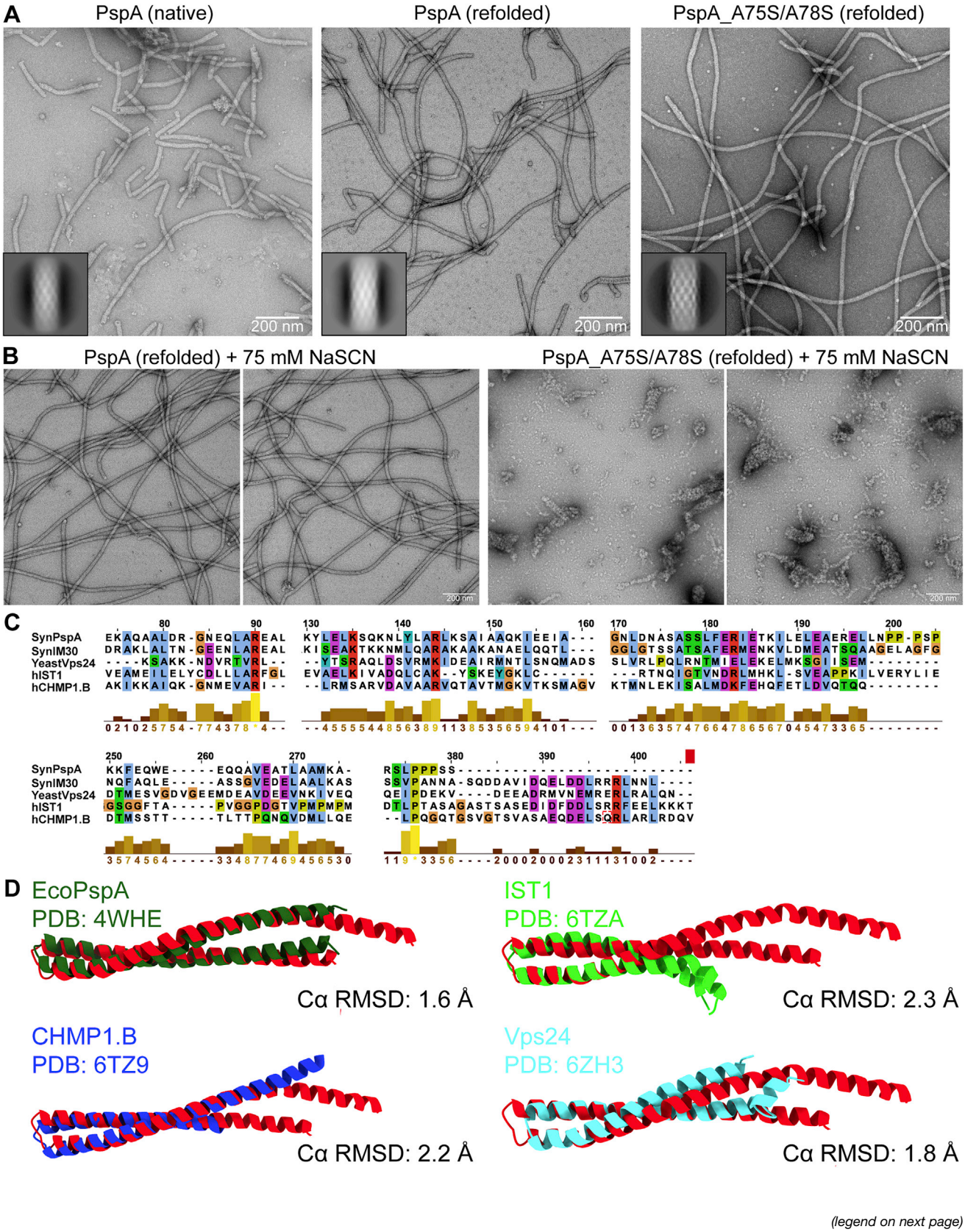

(legend on next page)

Figure S2. Negative staining electron micrographs of PspA and comparison of α1/α2 hairpin motif of PspA with eukaryotic ESCRT-III structures, related to Figures 2 and 4

(A) Micrographs of negatively stained samples of PspA after native extraction, and PspA as well as PspA_A75S/A78S after purification under denaturing conditions and subsequent refolding. The inset shows a representative 2D class average of each sample. (B) Micrographs of negatively stained samples of PspA and PspA_A75S/A78S after treatment with 75 mM NaSCN. After overnight dialysis against sodium phosphate buffer containing 75 mM NaSCN, rod formation is not affected in case of PspA wt, while formation of PspA_A75S/A78S rods is impaired. (C) Sequence alignment of PspA/IM30 with eukaryotic ESCRT-III proteins with bar graphs showing the alignment quality score as a measure of sequence similarity. Sequences were aligned using the T-Coffee webserver (Di Tommaso et al., 2011) and visualized with JalView (Waterhouse et al., 2009). (D) Structural superposition of the PspA hairpin with *Eco*PspA, IST1, CHMP1B and Vps24. Cα RMSD of residues approx. 50 – 90 (central hairpin) was calculated in Chimera using the "Match→Align" command.

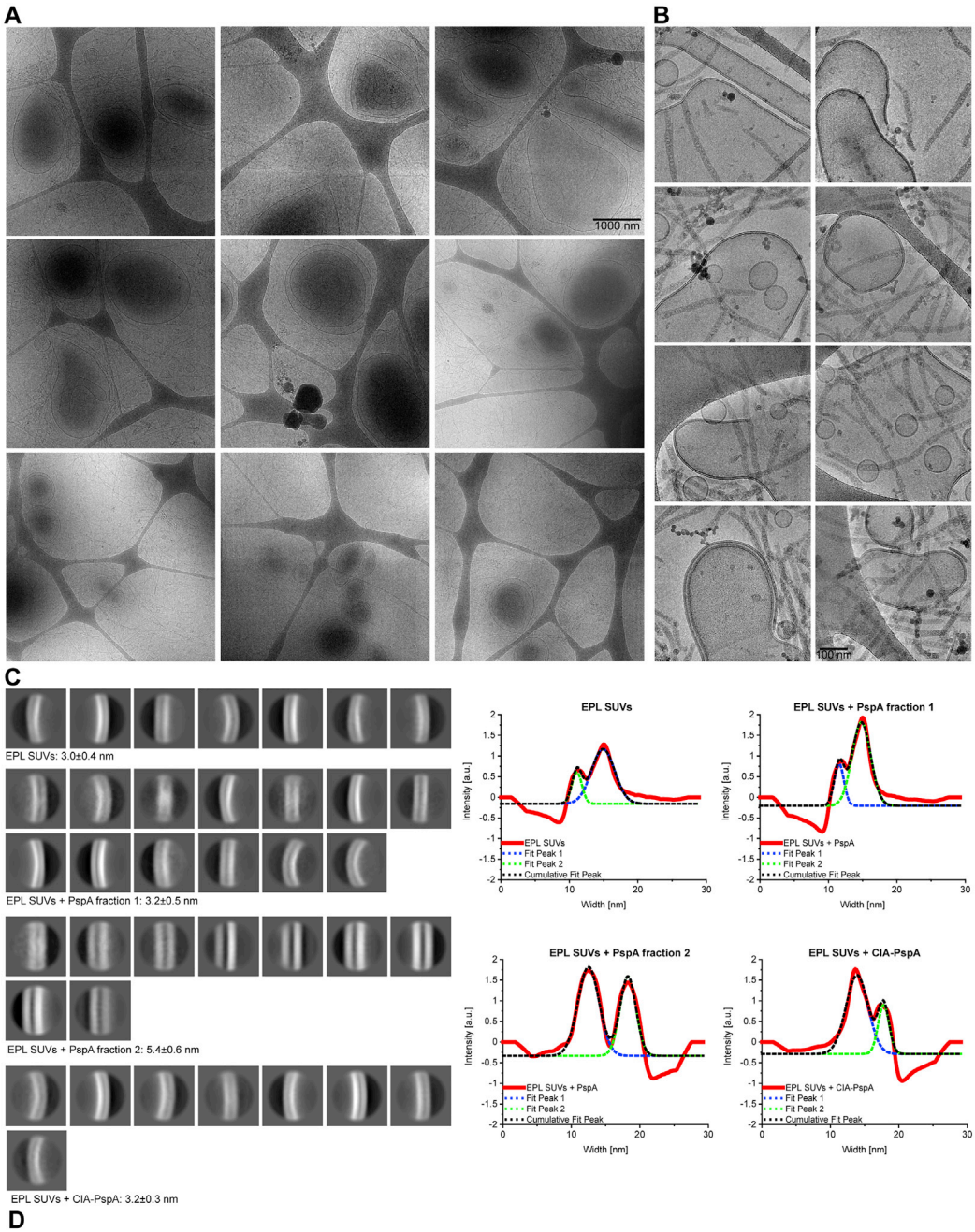

(legend on next page)

Figure S3. Gallery of cryo-micrographs showing *E. coli* polar lipids (EPL) small lamellar vesicles (SUVs) after incubation with PspA rods and image analysis, related to Figure 5

(A) Electron cryo-micrographs of EPL SUVs in the presence of PspA rods at low magnification. (B) EPL SUVs in the presence of PspA rods at high magnification. (C) Left. Class averages of bilayer segments of EPL, EPL+PspA and EPL+CIA. The average bilayer leaflet separation *d* denotes the average over all class averages per group with SD (n = number of the displayed class averages). Right. Representative density profiles of the respective class averages including the fitted peaks that were used to determine the bilayer leaflet separation. (D) Relative frequency of the determined bilayer leaflet separation based on the number of bilayer segments per class binned to 0.5 nm groups.

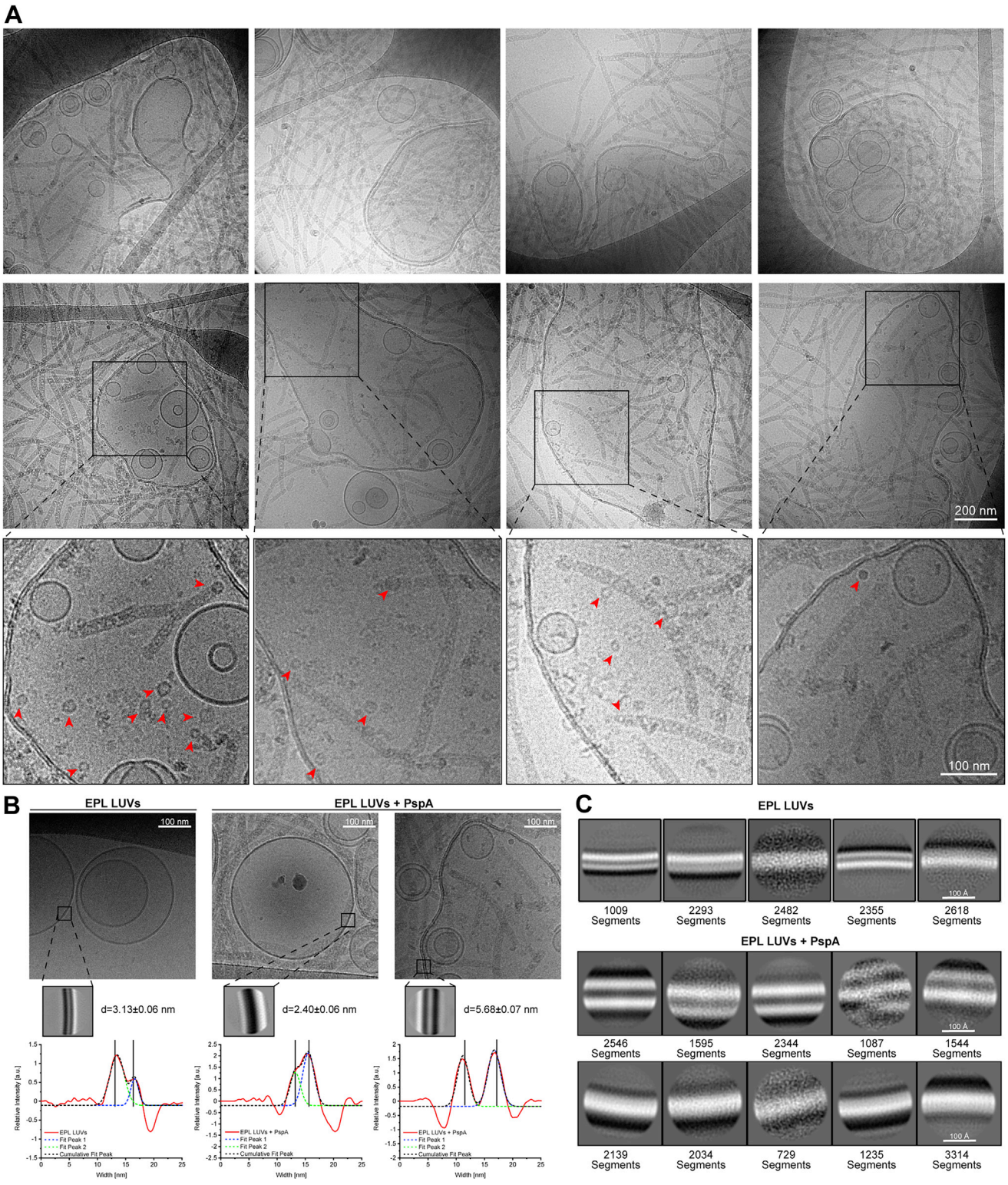

Figure S4. Gallery of cryo-micrographs showing *E. coli* polar lipid (EPL) large unilamellar vesicles (LUVs) after incubation with PspA rods and image analysis, related to Figure 5

(A) Electron cryo-micrographs of EPL LUVs in the presence of PspA rods at low magnification. Bottom row: magnified insets of the last row of LUV images. Red arrows indicate smaller oligomeric structures such as rings. (B) Top. In the absence of PspA, EPL large unilamellar vesicles (LUVs) are uniform and round, whereas

(legend continued on next page)

larger and deformed vesicles were observed in presence of PspA showing a distinct bilayer leaflet separation in addition to a fraction of unaltered uniform vesicles. Bottom. Detailed analysis of bilayer leaflet separation *d* in EPL vesicles determined from density profiles of class averages from segmented bilayers. Only class averages with clear features were used for the measurement. (n = 3 class averages, errors represent SD). (C) Class averages in absence and presence of PspA.

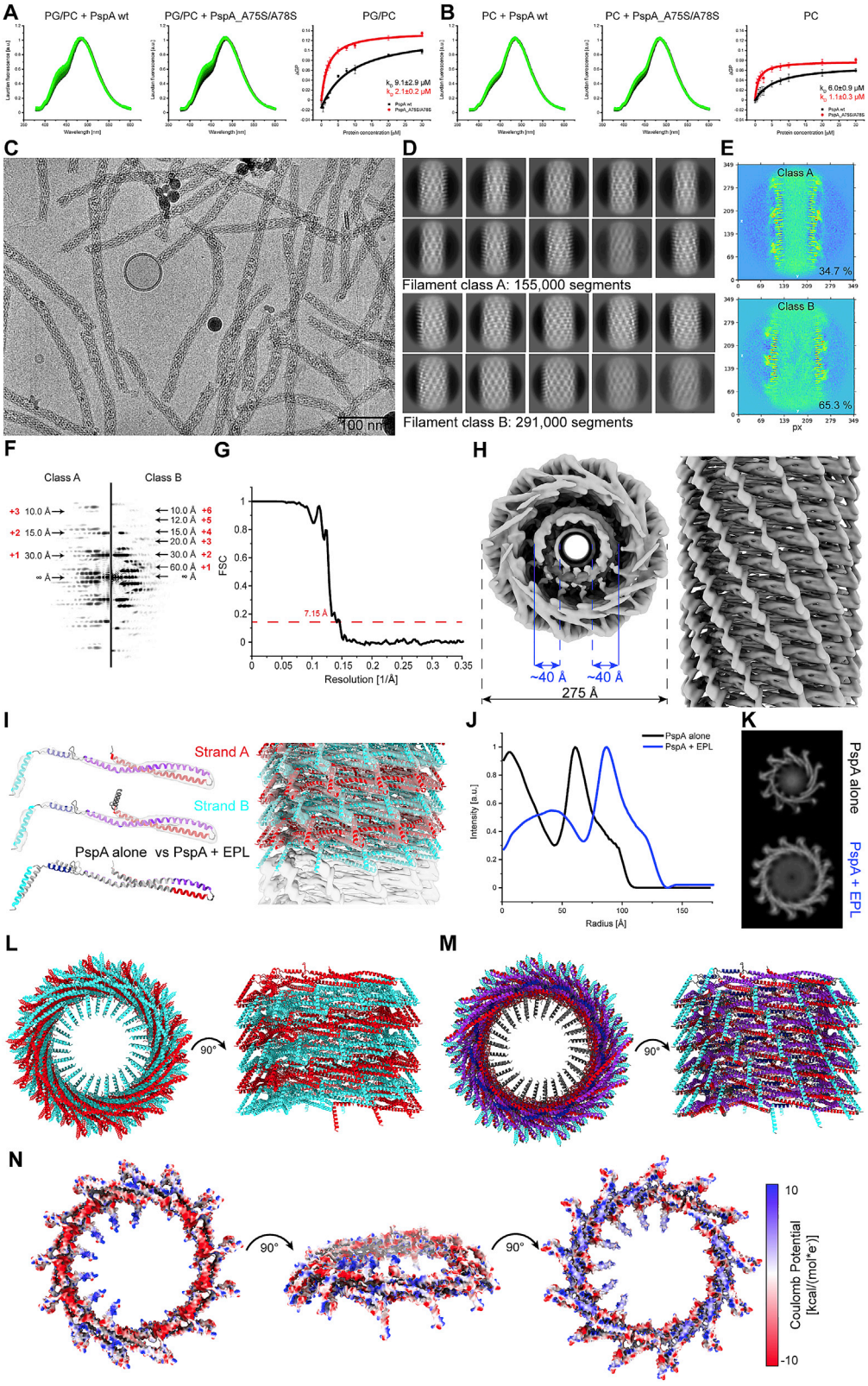

(legend on next page)

Figure S5. Membrane binding of PspA measured by fluorescence spectroscopy and cryo-EM structure of PspA rods in presence of EPL, related to Figure 5

(A and B) Laurdan fluorescence spectra for lipid binding of PspA wt and A75S/A78S to negatively charged DOPC/DOPG (60/40) (A) or net uncharged DOPC membranes (B). Spectra with increasing protein concentrations from 0 - 30 μM are shown (color coded with dark green to light green). Binding of PspA wt and mutant leads to an apparent increase in lipid order, indicated by the relative increase of the emission band around 440 nm. The binding curves constructed from the corresponding GP values show that binding of both variants is largely independent of the net membrane charge. Yet, both proteins have a slightly increased propensity to bind to negatively charged membranes, and the rod-destabilizing mutant binds with higher apparent affinity to membrane surfaces. An increase in lipid order induced by protein binding cannot be detected if the membrane is already largely in the ordered phase, thus this assay cannot be used to detect PspA binding to EPL liposomes. Error bars in the binding curves (right column) represent SE (n = 3). (C) Representative electron cryo-micrograph of PspA rods in the presence of EPL small unilamellar vesicles (SUVs). (D) Class averages of rods grouped in two classes. (E) y-z slice of the 3D reconstruction of each rod class. The percent value in the bottom-right location indicates the segment ratio contributing to the respective 3D reconstruction. (F) Power spectra of 2D class averages of the two rod classes (class A left, class B right) indicating layer lines up to 10 Å resolution. Red numbers represent the predicted Bessel order of each layer line. (G) Fourier shell correlation of rod class B indicating a 7.2 Å resolution at the 0.143 cutoff. (H) Top and side view of cryo-EM density of rod class B with measurement of the width and thickness of the inner density. (I) Left: segmented cryo-EM density superimposed on built model of PspA (strand A:22-217, strand B: 1-217) with colored α helices in ribbon presentation (α1: red, α2/α3: purple, α4: blue, α5: cyan) and comparison of the model of PspA alone versus PspA+EPL. Right: density of PspA+EPL rods with fitted helical assembly in side view. The assembly is a two-start helix with 4.4 Å rise and 26.6° twist (strand A in red, strand B in cyan). (J) Radial density profiles of PspA alone and PspA+EPL (class B) rods. (K) Corresponding top view projection of PspA alone and PspA+EPL (class B) rods that were used to determine radial density profiles. (L) Helical assembly of PspA+EPL in top and side view (strand A in red, strand B in cyan). (M) Helical assembly of the PspA+EPL rod in side and top view with colored α helices in ribbon presentation (α1: red, α2/α3: purple, α4: blue, α5: cyan). (N) Electrostatic surface potential of PspA+EPL rods. The assembly consists of two unique ends with basic and acidic surfaces and pronounced positively charged surface patches in the inner volume.

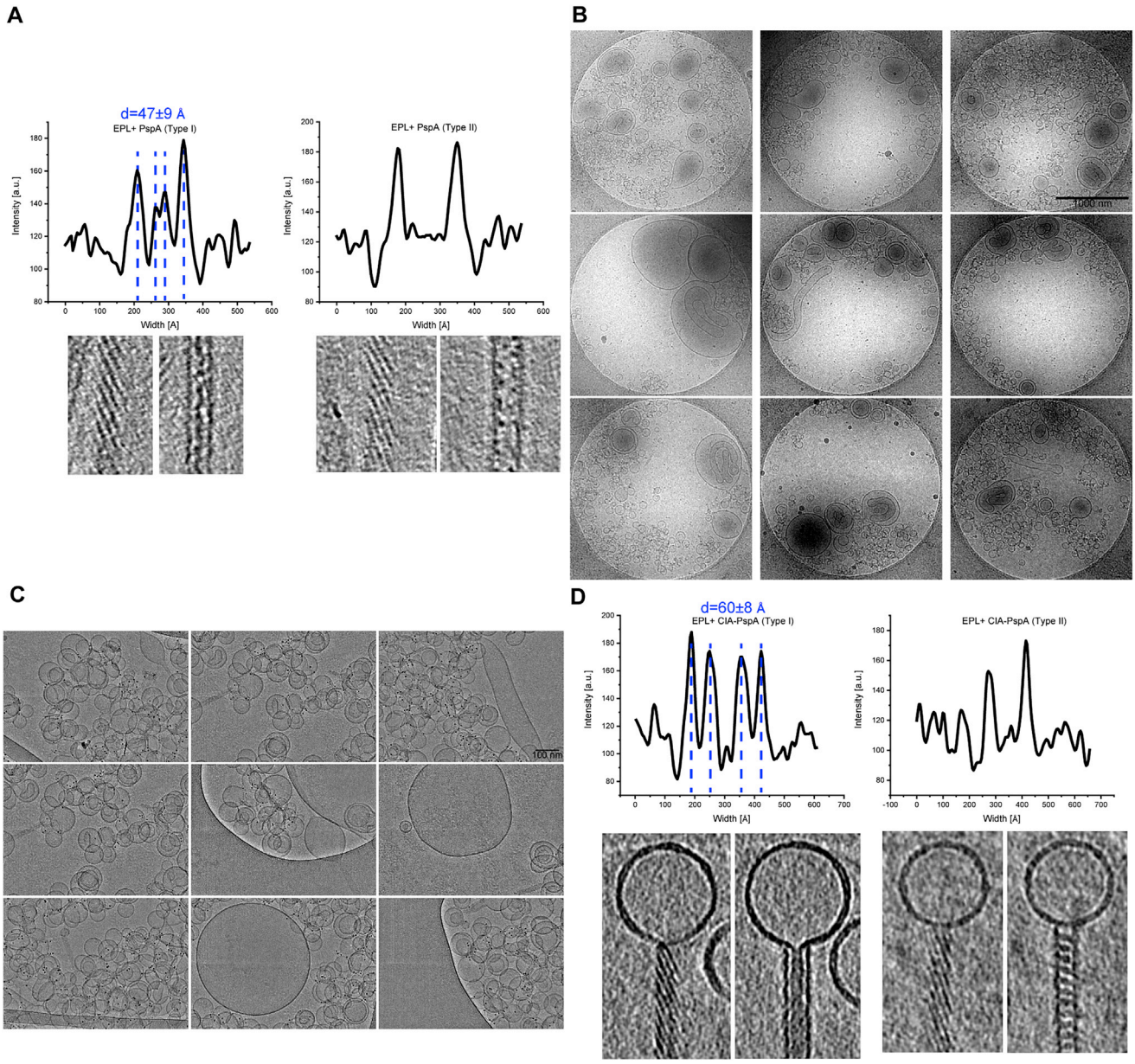

Figure S6. Density profiles of PspA rod tomogram slices and gallery of EPL SUVs after incubation with CIA-PspA, related to Figure 6

(A) Top: representative density profiles of PspA rods in the presence of EPL SUVs. Type I rod profiles show a distinct double-U pattern with peak-to-peak distances of 47 ± 9 Å (errors represent SD, n = 6), while the profiles of type II rods show a single-U pattern. Bottom: top and central tomogram slices of the respective rods. (B) Electron cryo-micrographs of EPL SUVs in the presence of CIA-PspA at low magnification. (C) EPL SUVs in the presence of CIA-PspA rods at high magnification. (D) Top: representative density profiles of CIA-PspA rods in the presence of EPL SUVs. Type I rod profiles show a pronounced double-U pattern with peak-to-peak distances of 60 ± 8 Å (errors represent SD, n = 8), while the profiles of type II rods show a single-U pattern. Bottom: top and central tomogram slices of the respective rods. The density of the observed double-U pattern is compatible with a lipid bilayer present in the inner lumen of the PspA rod.

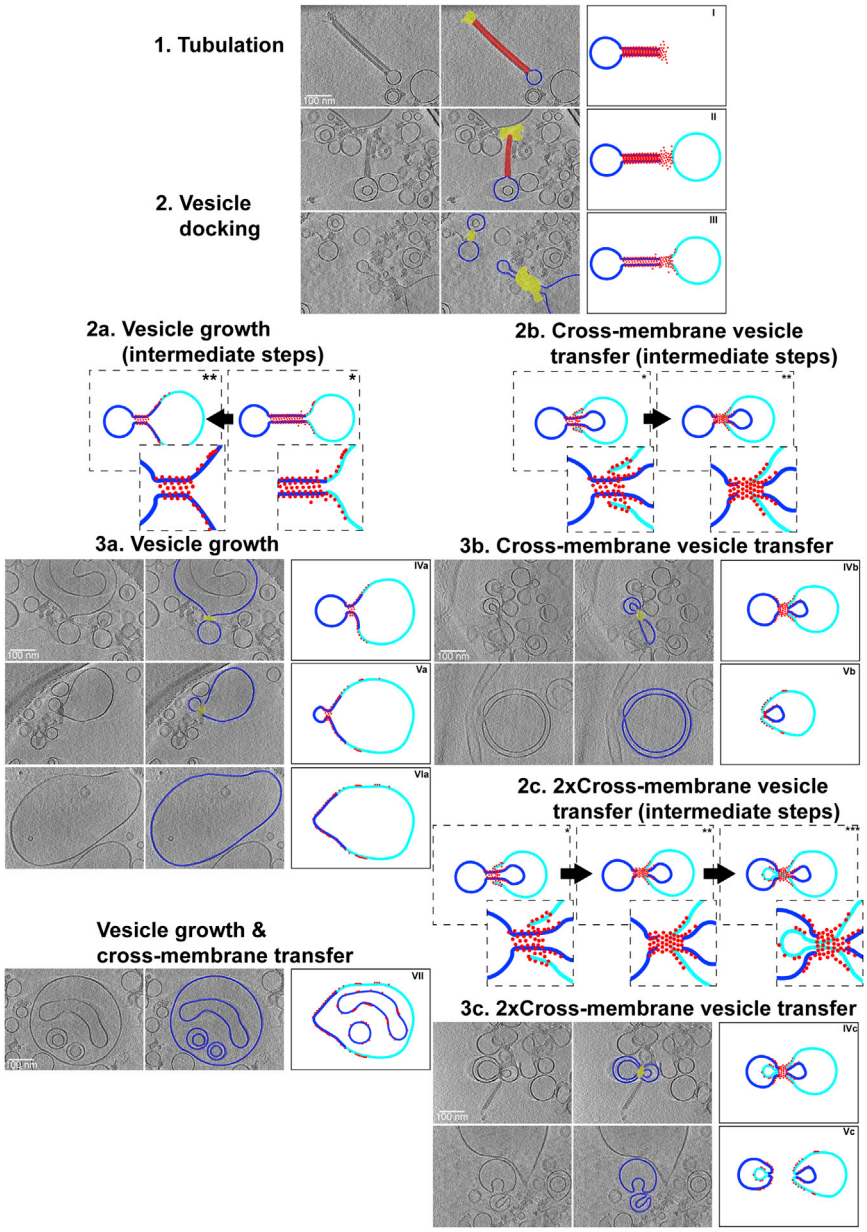

Figure S7. Detailed sequence of observed membrane topologies leading to a model of vesicle growth and cross-membrane vesicle transfer, related to Figure 7

A potential model of events leading to vesicle growth and cross-membrane vesicle transfer supported by cryo-EM images (Extended view of Figure 7). Left column: image slices of cryo-electron tomograms of PspA interacting with vesicles. Middle column: corresponding slices superimposed with 2D segmentation of the region of interest (rods in red, high-density zones in yellow and lipid bilayers in blue). Right column: simplified model (blue: donor membrane, cyan: acceptor membrane, red: PspA). For details see the main text.